

A Hubble Space Telescope Search for r -Process Nucleosynthesis in Gamma-ray Burst Supernovae

J. C. RASTINEJAD,¹ W. FONG,¹ A. J. LEVAN,^{2,3} N. R. TANVIR,⁴ C. D. KILPATRICK,¹ A. S. FRUCHTER,⁵ S. ANAND,⁶ K. BHIROMBHAKDI,⁵ S. COVINO,⁷ J. P. U. FYNBO,^{8,9} G. HALEVI,¹ D. H. HARTMANN,¹⁰ K. E. HEINTZ,^{8,9} L. IZZO,^{11,12} P. JAKOBSSON,¹³ T. KANGAS,^{14,15} G. P. LAMB,¹⁶ D. B. MALESANI,^{8,9,2} A. MELANDRI,¹⁷ B. D. METZGER,^{18,19} B. MILVANG-JENSEN,^{8,9} E. PIAN,²⁰ G. PUGLIESE,²¹ A. ROSSI,²² D. M. SIEGEL,^{23,24} P. SINGH,²⁵ AND G. STRATTA^{25,26,22,27}

¹Center for Interdisciplinary Exploration and Research in Astrophysics (CIERA) and Department of Physics and Astronomy, Northwestern University, Evanston, IL 60208, USA

²Department of Astrophysics/IMAPP, Radboud University, 6525 AJ Nijmegen, The Netherlands

³Department of Physics, University of Warwick, Coventry, CV4 7AL, UK

⁴School of Physics and Astronomy, University of Leicester, University Road, Leicester, LE1 7RH, UK

⁵Space Telescope Science Institute, 3700 San Martin Drive, Baltimore, MD 21218, USA

⁶Cahill Center for Astrophysics, California Institute of Technology, Pasadena CA 91125, USA

⁷INAF-Osservatorio Astronomico di Brera, Via Bianchi 46, I-23807, Merate (LC), Italy

⁸Cosmic DAWN Center, Denmark

⁹Niels Bohr Institute, University of Copenhagen, Jagtvej 155, 2200 Copenhagen N, Denmark

¹⁰Department of Physics and Astronomy, Clemson University, Clemson, SC 29634-0978, USA

¹¹INAF-Osservatorio Astronomico di Capodimonte, Salita Moiariello 16, I-80131, Napoli, Italy

¹²DARK, Niels Bohr Institute, University of Copenhagen, Jagtvej 155, 2200 Copenhagen N, Denmark

¹³Centre for Astrophysics and Cosmology, Science Institute, University of Iceland, Dunhagi 5, 107, Reykjavik, Iceland

¹⁴Finnish Centre for Astronomy with ESO (FINCA), FI-20014 University of Turku, Finland

¹⁵Tuorla Observatory, Department of Physics and Astronomy, FI-20014 University of Turku, Finland

¹⁶Astrophysics Research Institute, Liverpool John Moores University, IC2 Liverpool Science Park, 146 Brownlow Hill, Liverpool, L3 5RF, UK

¹⁷INAF-Osservatorio Astronomico di Roma, Via di Frascati 33, I-00078, Monte Porzio Catone (RM), Italy

¹⁸Department of Physics and Columbia Astrophysics Laboratory, Columbia University, Pupin Hall, New York, NY 10027, USA

¹⁹Center for Computational Astrophysics, Flatiron Institute, 162 5th Ave, New York, NY 10010, USA

²⁰INAF, Astrophysics and Space Science Observatory, Via P. Gobetti 101, 40129 Bologna, Italy

²¹Astronomical Institute Anton Pannekoek, University of Amsterdam, 1090 GE Amsterdam, The Netherlands

²²INAF - Osservatorio di Astrofisica e Scienza dello Spazio, via Piero Gobetti 93/3, 40129 Bologna, Italy

²³Institute of Physics, University of Greifswald, D-17489 Greifswald, Germany

²⁴Department of Physics, University of Guelph, Guelph, Ontario N1G 2W1, Canada

²⁵Institut für Theoretische Physik, Goethe Universität, Max-von-Laue-Str. 1, 60438 Frankfurt am Main, Germany

²⁶INAF - Istituto di Astrofisica e Planetologia Spaziali, via Fosso del Cavaliere 100, I-00133 Roma, Italy

²⁷INFN - Roma 1, Piazzale Aldo Moro 2, 00185, Roma

ABSTRACT

Simulations and indirect observational evidence have suggested that, in addition to the mergers of compact objects, there exists a secondary source of heavy element (r -process) nucleosynthesis with a short delay from star formation: the core-collapse of rapidly-rotating and/or highly-magnetized massive stars. Here, we probe a predicted signature of r -process enrichment, a late-time ($\gtrsim 40$ days post-burst) distinct red color, in observations of GRB-supernovae (GRB-SNe) which are linked to these massive star progenitors. We present optical to near-IR color measurements of four GRB-SNe at $z \lesssim 0.4$, extending out to > 500 days post-burst, obtained with the *Hubble Space Telescope* and large-aperture ground-based telescopes. Comparison of our observations to models indicates that GRB 190829A favors little ($\leq 0.01M_{\odot}$) r -process enrichment whereas GRB 100316D is consistent with producing $0.03 - 0.15M_{\odot}$ of r -process material. Observations of GRBs 030329 and 130427A are not on sufficient timescales to robustly constrain enrichment, although taken together the sample of GRB-SNe

indicates color diversity at late times. Our sample also disfavors large amounts of mixing between the inner r -process ejecta and outer SN layers. Our derived yields from GRB-SNe may be underestimated due to r -process material hidden in the SN ejecta (potentially due to low mixing fractions) or the limits of current models in measuring r -process mass. We conclude with recommendations for future search strategies to observe and probe the full distribution of r -process produced by GRB-SNe.

Keywords: gamma-ray bursts, supernovae, r -process

1. INTRODUCTION

For decades, the formation sites for many of the Universe’s heaviest elements, including many of those that enable life on Earth such as Thorium and Iodine, remained unknown. These elements are widely believed to form via rapid neutron capture (“ r -process”) nucleosynthesis (Burbidge et al. 1957; Cameron 1957). This process requires origin sites capable of producing high neutron abundance fractions that are common enough to create the observed abundances within a Hubble time. The traditional core-collapse of massive stars, in which neutronization of material close to the remnant (e.g., Cowan et al. 1991; Woosley et al. 1994; Hoffman et al. 1997; Thielemann et al. 2011; Cowan et al. 2021), was initially proposed as an origin site but recently has fallen out of favor (as discussed further below). Binary neutron star (BNS) or neutron star-black hole mergers, in which a high neutron fraction is naturally achieved through tidal stripping of the outer layers of the neutron star in the final orbits before merging (e.g., Lattimer & Schramm 1974; Rosswog et al. 1999) or through outflows from the post-merger accretion disk (e.g., Metzger et al. 2009) became the favored channel to produce r -process elements. In 2017, BNS mergers were confirmed to produce at least a fraction of the Universe’s r -process elements with the first BNS merger detected through gravitational waves (GW170817; Abbott et al. 2017a), coincident short gamma-ray burst (GRB 170817A; Abbott et al. 2017b; Goldstein et al. 2017; Savchenko et al. 2017) and thermal kilonova AT2017gfo (Arcavi et al. 2017; Coulter et al. 2017; Lipunov et al. 2017; Tanvir et al. 2017; Soares-Santos et al. 2017; Valenti et al. 2017).

Despite the spectacular confirmation of r -process in BNS mergers, it remains an open question as to whether other heavy element formation channels are needed to explain the mass and abundance pattern of r -process elements observed in our Solar System. Indirect evidence in the form of early heavy element enrichment in our Galaxy provides a convincing argument for a site tied to the collapse of massive stars (e.g., Côté et al. 2017; Hotokezaka et al. 2018; Naidu et al. 2022). Observations of r -process-enhanced metal-poor stars in the Milky Way, some ultra-faint dwarf galaxies (e.g., Ji et al.

2016; Hansen et al. 2017; Frebel 2018), and globular clusters (e.g., Zevin et al. 2019; Kirby et al. 2020, 2023) suggest the existence of a heavy element formation channel with a short delay from star formation (Kirby et al. 2023 find a delay $\lesssim 0.8$ Myr). Current estimates of the minimum delay time of BNS mergers, inferred from short GRB host galaxy offsets, stellar population ages, and star formation histories (e.g., Fong et al. 2022; Nugent et al. 2022; O’Connor et al. 2022; Zevin et al. 2022; Nugent et al. 2023) and predicted by simulations (e.g., Belczynski et al. 2002; Dominik et al. 2012; Tauris et al. 2017; Mandhai et al. 2022) remain uncertain, but it is unlikely that these events can provide a ubiquitous r -process enrichment source as quickly as massive star channels.

Core-collapse SNe (CCSNe), associated with the deaths of massive stars and the formation of compact objects, provide a natural source with a short delay from star formation (on a stellar evolutionary timescale). In the 1990s, it was hypothesized that ordinary, jet-less CCSNe could produce neutron-rich material due to the high-entropy neutrino wind formed around the proto-neutron star remnant (e.g., Woosley et al. 1994). However, high event rates and observations of ordinary CCSNe have led to a general consensus that these events do not significantly contribute to the Universe’s r -process budget (Macias & Ramirez-Ruiz 2018; Wallner et al. 2015, 2021; although see Tsujimoto & Shigeyama 2001 who find that SN 1987A’s Ba/Sr ratio is more consistent with r -process than slow neutron capture, s -process). In addition, simulations have struggled to create or eject any neutron-rich material before accretion onto the remnant object (e.g., Arcones et al. 2007; Fischer et al. 2010; Martínez-Pinedo et al. 2012, 2014).

One suggested CCSNe source that could potentially decrease the event rates and overcome the ejection problem is magneto-rotational (jet-driven) SNe (MR SNe or magneto-rotational hypernovae). In these MR SNe, rapid rotation of the iron core amplifies the magnetic field (e.g., Cameron 2003; Mösta et al. 2015) launching jets and subsequent magneto-centrifugal winds (e.g., Thompson et al. 2004; Metzger et al. 2007) that provide a mechanism to eject neutron-rich material. More re-

cent simulations of MR SNe have found that strong and efficient magnetic fields are critical for this pathway to the r -process, though it is unknown how common magnetic fields of this strength are in nature (e.g., Halevi & Mösta 2018; Mösta et al. 2018; Thompson & ud-Doula 2018). At present, few models for observational signatures of r -process produced through the MR SN production channel have been published (e.g., Reichert et al. 2023).

Recently, Siegel et al. (2019) demonstrated that accretion disks following rapidly-rotating massive stars undergoing core-collapse (“collapsars”) may also create and successfully eject r -process elements. Using magnetohydrodynamic (MHD) simulations they determined that the post-collapse disk favors weak interactions that produce neutron-rich material capable of synthesizing the heaviest elements. Their simulations also demonstrate that heating due to the disk’s magnetic turbulence is sufficient to unbind the neutron-rich material, ejecting material in winds that will undergo the r -process, mix with the associated SN’s outer layers and produce a red color signature analogous to the reddening of a kilonova (though on longer timescales; Siegel et al. 2019; Zenati et al. 2020). Additional simulations have further explored the dependency of r -process yields on neutrino treatment and accretion rate, and have disfavored collapsars as sources of heavy (e.g., lanthanide-rich) r -process material (Miller et al. 2020; Fujibayashi et al. 2022; Just et al. 2022). However, given the uncertainties on these parameters (e.g., assumed range of accretion rates, treatment of disk viscosity, assumed stellar structure and rotation profiles of progenitor models), r -process enrichment from collapsars remains plausible. Barnes & Metzger (2022) develop a semi-analytic light curve model for collapsar SNe enriched with r -process, which predicts their photometric color evolution for sufficiently large r -process enrichment levels. Their models produce a distinguishable red excess that emerges several weeks to months following the initial explosion. The model suite spans a range of r -process enrichment masses and degrees of mixing between the inner disk ejecta and SN outer layers, which imprint themselves on the light curves in the form of distinct optical to near-IR (NIR) colors.

Despite extensive work on the theoretical end, few observational searches have been performed for r -process enhancement in SNe associated with collapsars. Searches for radio flares following long-duration GRBs (typically the product of collapsars) have been performed, a possible signature of interaction of the collapsar’s wind ejecta with the surrounding medium (Lee et al. 2022). While no late-time radio flares

were uncovered, there are several potential alternate sources that could explain radio emission in the event of such a discovery. Additionally, the high and sustained photospheric velocities inferred from observations of SN 2020bvc have been interpreted as power by a heavy element mixing source such as the r -process (Li et al. 2023). However, there are no signs of reddening in the SN light curve.

Anand et al. (2023) perform a comprehensive search for r -process signatures in collapsar SNe using contemporaneous optical-NIR color measurements for a sample of 25 nearby broad-lined, stripped-envelope SNe (SNe Ic-BL) mostly discovered by the Zwicky Transient Facility (including one associated with a GRB, GRB 190829A). Their sample of SNe Ic-BL light curves was best fit by r -process-free models and favors no or low r -process yields from nearby SNe Ic-BL detected mostly without GRBs.

The SNe Ic-BL associated with long GRBs (GRB-SNe) are generally considered the best targets for observable r -process enrichment in collapsars, in part due to the high angular momentum required to produce large accretion disks capable of launching the GRB jet (e.g., MacFadyen & Woosley 1999; Siegel et al. 2019; Barnes & Duffell 2023). In addition, Barnes & Duffell (2023) find that GRB jets are likely to increase mixing between the inner r -process ejecta and the outer layers, thus producing a more prominent red color. As this effect is likely enhanced closer to the jet axis, GRB-SNe, which have relatively pole-on orientations, are strong candidates for observing r -process signatures. Blanchard et al. (2023) do not find signs of r -process enrichment from a late-time NIR spectrum of the SN counterpart to GRB 221009A, though this observation was complicated by a bright afterglow.

The absence of a previous search for photometric signatures of r -process enrichment in a sample of GRB-SNe is in part due to the low rates of events within the requisite volume to detect the faint signatures (e.g., $z \lesssim 0.4$). For many past low-redshift events, no published late-time NIR data exists. The paucity of these measurements reflects the NIR sensitivity often required to study even low-redshift SNe on the timescales of these signatures ($30 \lesssim \delta t \lesssim 300$ days, where δt is the time since the GRB trigger).

Here, we provide late-time *Hubble Space Telescope* (*HST*) and large-aperture ground-based color measurements for a sample of four nearby GRB-SNe extending to $\gtrsim 500$ days following the GRB trigger. In Section 2 we describe our sample selection and detail the observations. In Section 3 we describe our process of ascertaining the intrinsic SNe colors. In Section 4 we compare

our observations to the r -process enriched SNe models of Barnes & Metzger (2022). In Section 5 we review the implications of our work and discuss future observing strategies. Throughout, we assume a cosmology of $H_0 = 69.6 \text{ km s}^{-1} \text{ Mpc}^{-1}$, $\Omega_M = 0.286$, $\Omega_{vac} = 0.714$ (Bennett et al. 2014) and report magnitudes in the AB system.

2. OBSERVATIONS

2.1. Sample Selection and Data Description

As a starting point, we utilize the comprehensive GRB-SNe compilation of Dainotti et al. (2022), which includes 58 long-duration GRBs with claimed SNe observed from 1990–2021. Following our motivation to identify NIR photometric excesses in the SN light curve due to the presence of r -process material, we narrow this sample to GRB-SNe events (i) for which late-time ($\delta t \gtrsim 30$ days), nearly simultaneous optical-NIR observations are available, (ii) identified after the discovery of SN 1998bw, as we do not expect previous GRB-SNe to have well-sampled light curves, (iii) at $z < 0.4$, the approximate distance out to which *HST* is capable of observing the predicted color evolution of r -process enriched GRB-SNe, and (iv) not associated with a putative kilonova (e.g., GRBs 211211A and 230307A; Rastinejad et al. 2022; Troja et al. 2022; Yang et al. 2022; Gillanders et al. 2023; Levan et al. 2023a; Yang et al. 2023). Applying these criteria, our final sample comprises four GRB-SNe: GRB 030329 (SN 2003dh), GRB 100316D (SN 2010bh), GRB 130427A (SN 2013cq), and GRB 190829A (SN 2019oyw). We also considered but ultimately did not include GRB 221009A in our sample, due to a combination of high Galactic extinction (e.g., Williams et al. 2023), sparse late-time sampling of observations, and afterglow contamination in early *HST* epochs (Levan et al. 2023b). We list the basic properties of these bursts in Table 1 and describe each GRB and our data reduction further in Sections 2.2–2.5. Throughout this work, we refer to each event, including the SN, with its GRB name.

In total, we collect 79 *HST* observations obtained with the Advanced Camera for Surveys (ACS) Wide Field Channel (WFC), Wide Field Camera 3 (WFC3) Ultraviolet-Visible (UVIS) and Infrared (IR) channels, and the Near Infrared Camera and Multi-Object Spectrometer (NICMOS) Camera 2 (NIC2) instruments from the MAST archive¹ and the Hubble Legacy Archive (HLA)². The observations span $8 < \delta t < 969$ days

post-burst (including template observations) and seven *HST* filters (Table 1). We also collect and reduce VLT/X-shooter (acquisition camera), VLT/HAWK-I and MMT/Binospec observations of GRB 190829A (Section 2.5). With the exception of the NICMOS/NIC2 imaging, all reported photometry is performed on image subtractions with a late-time ($\delta t \gtrsim 420$ days) template (see Section 2.6 for further discussion on potential template contamination). In Figure 1 we show representative *HST* images where the SN is detected (left column) and the template image used for image subtraction (right column). We report all photometry in Table 2 and plot the observations in Figure 2. In Section 3.1 we discuss our corrections for Galactic and local dust extinction.

To complement the photometry analyzed in this work, we gather additional relevant data from the literature. As our goal is to compare the optical-NIR color evolution of the GRB-SNe in our sample to relevant models, we collect only host-subtracted photometry in the $rRiIJHK$ -bands of GRBs 030329 (Matheson et al. 2003), 100316D (Olivares E. et al. 2012), 130427A (Perley et al. 2014) and 190829A (Hu et al. 2021). This results in an additional 519 observations from the literature. The vast majority of these measurements occur at $0.1 \lesssim \delta t \lesssim 40$ days, extending our dataset at early times.

2.2. GRB 030329

GRB 030329 was discovered by the High Energy Transient Explorer II (HETE-II) at 11:14:14.67 UT on 29 March 2003 with a duration of 21 s (Vanderspek et al. 2003). A bright optical afterglow counterpart was quickly localized. The burst’s redshift of $z = 0.1685$ was identified through afterglow spectroscopy (Greiner et al. 2003). Subsequent spectroscopic and photometric observations of the counterpart revealed evidence of an SN Ic-BL (Hjorth et al. 2003; Kawabata et al. 2003; Matheson et al. 2003; Mazzali et al. 2003; Stanek et al. 2003; Lipkin et al. 2004).

GRB 030329 was observed with ACS/WFC in the F606W and F814W filters at several nearly contemporaneous epochs (within ≈ 24 hours) over $17 \lesssim \delta t \lesssim 228$ days, and at $\delta t = 428$ days in F606W only (Program 9405; PI: Fruchter). We download the flat-fielded, dark-subtracted and CTE-corrected images and combine them using *astrodrizzle* (Gonzaga et al. 2012) with a pixel scale of $0.05''$. We note that while the F814W image observed on 12 November 2003 was partially contaminated by internally scattered light from the WFPC2 internal lamp, the position of the SN is not affected by the uneven background.

¹ <https://mast.stsci.edu/search/ui/#/hst>

² <https://hla.stsci.edu>

Table 1. GRB Sample & Properties

GRB	SN	$T_{90,\text{rest}}^\dagger$ (s)	z	$A_{V,\text{MW}}$ (mag)	$E(B-V)_{\text{loc}}$ (mag)	HST Observed Filters [‡]	Program ID(s)
030329	2003dh	18	0.1685	0.069	0.04 ¹	F606W, F814W, F110W, F160W	9405
100316D*	2010bh	261	0.0591	0.319	0.14 ²	F555W, F814W, F125W, F160W	11709, 12323
130427A	2013cq	182	0.3399	0.055	0.05 ³	F606W, F160W	13110, 13117, 13230, 13951
190829A	2019oyw	49	0.0785	0.133	1.04 ⁴	F606W, F110W, F140W, F160W	15089, 15510, 16042, 16320

NOTE— [†] T_{90} duration as seen by *Swift*, except for GRB030329 which was observed by HETE-II, converted to the rest frame using the redshifts listed here.

[‡] Filters selected based on data availability on timescales relevant for observing r -process-enriched component (contemporaneous colors observed at $\delta t \gtrsim 30$ days).

* Low-luminosity GRB.

Milky Way extinction values are taken from Schlafly & Finkbeiner (2011).

References: (1) Matheson et al. (2003); (2) Bufano et al. (2012); (3) Levan et al. (2014a); (4) Chand et al. (2020).

We perform subpixel alignments between coadded images using `tweakreg` (Gonzaga et al. 2012) and align in image coordinates using standard IRAF tasks. We employ HOTPANTS (Becker 2015), which uses point-spread function (PSF) convolution, and IRAF/`imarith` for image subtraction. In general, the subtraction methods produce consistent photometry. We use HOTPANTS as our default image subtraction software throughout this work as it often produces higher signal-to-noise residuals than `imarith`, likely because of the treatment of the slight variations in PSF due to focus and orientation changes. In select cases we find that HOTPANTS does not produce realistic residuals, motivating us to employ `imarith`. For each residual image, we detect a $\gtrsim 3\sigma$ residual consistent with the position of the SN (Matheson et al. 2003) in the subtractions. We utilize the tabulated *HST* zeropoints to calibrate our images and perform aperture photometry with a 3–4 pixel aperture on the subtracted images (corresponding to $\sim 1 \times \text{FWHM}$), accounting for the appropriate encircled energy corrections (Bohlin 2016).

GRB030329 was also observed in the F110W and F160W filters with NICMOS/NIC2 at $\delta t \approx 17, 23, 44$ and 228 days. We download the drizzled images from the HLA. We discard the F110W and F160W images observed at $\delta t = 17$ days due to saturation of the SN. As noted in previous works, these images suffer from known artifacts (Östlin et al. 2008) and have a narrow field-of-view, preventing robust alignment and thus, reliable image subtraction. Thus, we perform relative photometry to obtain our measurements by subtracting the flux of the host galaxy in the epoch at $\delta t = 228$ days from those in each of the initial three epochs. We cor-

rect our photometry for the NICMOS/NIC2 encircled energy corrections listed in the NICMOS Handbook³.

2.3. GRB 100316D

The sub-energetic, low-luminosity GRB 100316D was discovered with the Neil Gehrels *Swift* Observatory (*Swift*; Gehrels et al. 2004) at 12:44:50 UT on 16 March 2010. The burst duration was 277 s and its spectrum was noticeably soft (Sakamoto et al. 2010). The Swift X-Ray Telescope (XRT) promptly identified and localized an X-ray counterpart. Shortly thereafter, multiple telescopes observed an optical counterpart embedded in a galaxy at $z = 0.0591$ (e.g., Chornock et al. 2010; Starling et al. 2011). Spectroscopic features of a SN Ic-BL were observed in the optical counterpart a few days following the initial trigger (Chornock et al. 2010; Starling et al. 2011; Bufano et al. 2012; Olivares E. et al. 2012).

GRB 100316D was observed with WFC3/UVIS in the F555W and F814W filters, and with WFC3/IR in the F110W and F160W filters (Programs 11709, 12323; PI: Bersier) over $8 \lesssim \delta t \lesssim 505$ days. We reduce the *HST* data in the same manner as described in Section 2.2. We perform image subtraction for each epoch using HOTPANTS and photometry on the HOTPANTS residual images using a 3–4 pixel aperture ($\sim 1 - 2 \times \text{FWHM}$) and account for the appropriate encircled energy corrections⁴. We note that the SN in the F125W and F160W images on 4 April 2010 ($\delta t \approx 16$ days) is saturated and we do not include these images in our analysis. We find our early photometry is in reasonable agreement

³ <https://www.stsci.edu/hst/instrumentation/legacy/nicmos>

⁴ www.stsci.edu/hst/instrumentation/wfc3/data-analysis/photometric-calibration/uvic-encircled-energy
www.stsci.edu/hst/instrumentation/wfc3/data-analysis/photometric-calibration/ir-encircled-energy

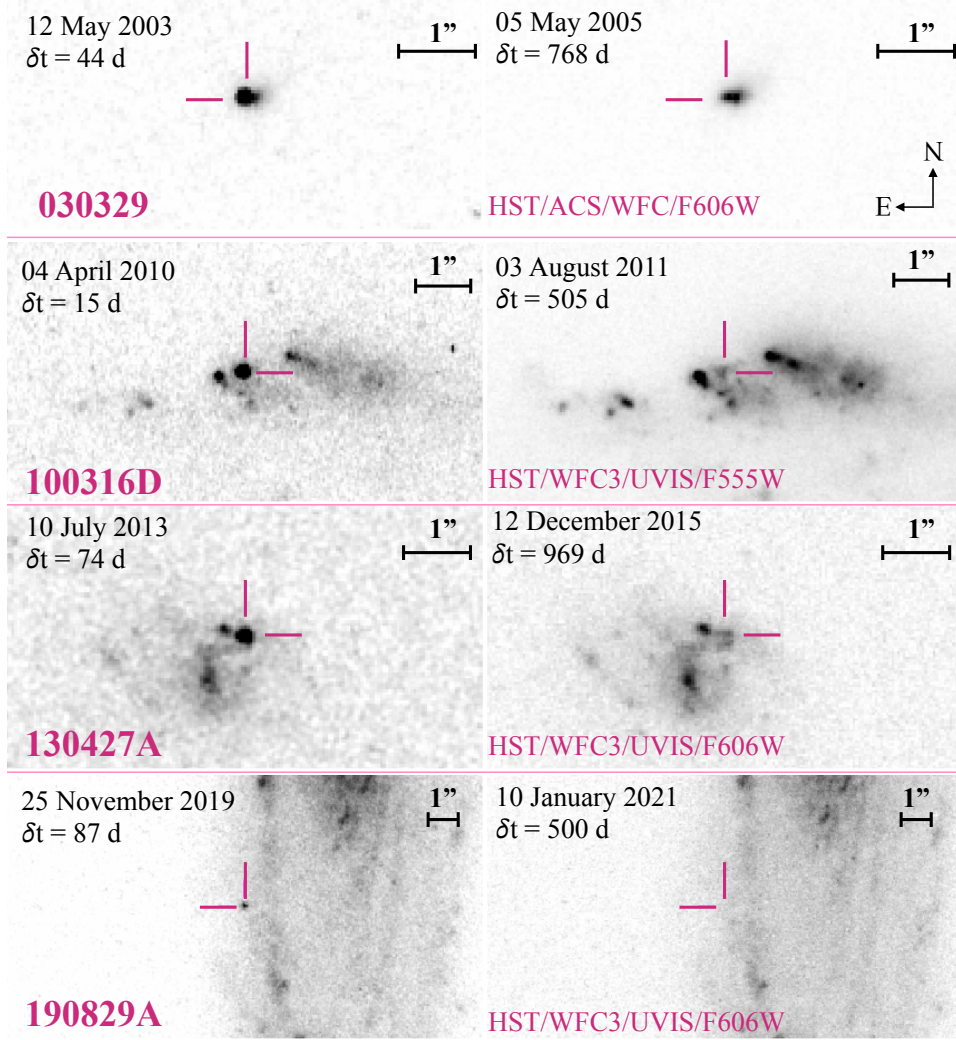


Figure 1. Example *HST* images of the fields of the four GRBs in our sample in which the SN is detected (left) and the late-time templates (right). In each panel we show the position of the SN with pink crosshairs and note the time since GRB detection. We do not expect the SN or afterglow to be significantly contributing to any of our templates, with the potential exception of GRB 130427A in F160W (see Section 2.6).

with the analysis of this data reported in Cano et al. (2011). At $\delta t \gtrsim 24$ days, we find our values are fainter by $\sim 0.3\text{--}1.2$ mag compared to their values. This difference can be ascribed to our process of image subtraction in comparison to their direct photometry on the host-embedded SN (Cano et al. 2011).

2.4. GRB 130427A

GRB 130427A was detected by *Swift* and the *Fermi* Space Telescope (*Fermi*; Meegan et al. 2009) on 27 April 2013 at 07:47:06.42 UT. Its gamma-ray properties were unprecedented: at the time, the GRB had the highest observed fluence and most energetic photon recorded to date (von Kienlin 2013; Ackermann et al. 2014; holding the fluence record until the recent discovery of GRB 221009A; e.g., Burns et al. 2023). The

burst duration as seen by *Swift* was 244 s. Prompt optical afterglow spectroscopy identified the GRB at $z = 0.3399$ (Levan et al. 2013) and multi-wavelength follow-up revealed an extraordinarily luminous afterglow (e.g., Laskar et al. 2013; Maselli et al. 2014; Perley et al. 2014). Spectroscopy of the counterpart revealed an associated SN Ic-BL (Xu et al. 2013; Melandri et al. 2014; Levan et al. 2014a).

GRB 130427A was observed with ACS/WFC and WFC3/UVIS in the F606W filter and WFC3/IR in the F160W filter for 7 contemporaneous epochs over $74 \lesssim \delta t \lesssim 969$ days (Programs 13110, 13117, 13230, 13951; PIs: Fruchter, Levan). We perform image subtractions between the initial six observations and the template image observed at $\delta t = 969$ days, then perform photometry on the residual with a 3 pixel aperture.

Due to striping on the F160W image observed on 2014 December 5, we do not see a $\gtrsim 3\sigma$ significant residual and discard the image. For all other epochs, we perform photometry at the position of the residual with a 3 pixel aperture and correct for the encircled energy.

2.5. GRB 190829A

GRB 190829A was identified by the *Swift*, *Fermi* and Konus-Wind satellites on 29 August 2019 at 19:55:53 UT (time as discovered by *Fermi*) and promptly localized to a galaxy with a known redshift of $z = 0.0785$ (Dichiara et al. 2019; *Fermi* GBM Team 2019; Tsvetkova et al. 2019). The burst had a gamma-ray duration of 53 s. The early afterglow was detected across the electromagnetic spectrum (e.g., Rhodes et al. 2020; H. E. S. S. Collaboration et al. 2021; Dichiara et al. 2022), and later spectroscopic observations revealed features consistent with an SN Ic-BL (Hu et al. 2021; Anand et al. 2023).

GRB 190829A was observed with *HST* with WFC3/UVIS in F606W and WFC3/IR in F140W over six contemporaneous epochs spanning $87 \lesssim \delta t \lesssim 500$ days (Programs 15510, 16042, 16320; PIs: Levan, Tanvir). We also incorporate early ($29 < \delta t < 58$ days) images observed in the F110W and F160W filters (Program 15089; PI: Troja). We download, combine and align the F606W and F140W images using the procedure described above, and perform image subtractions with HOTPANTS. A residual at the SN position is detected at $\gtrsim 3\sigma$ significance in all subtracted images. We perform photometry on all residual images (and directly on the F110W and F160W images as host contamination is insignificant at these epochs) with a 3–4 pixel aperture and correct for the encircled energy using the tabulated values.

In addition, we present VLT and MMT imaging of GRB 190829A observed over $25.4 < \delta t < 141$ days. VLT observations were obtained in the r -band with the X-shooter acquisition camera and in the JHK_s -band with the HAWK-I instrument (Programs 0103.D-0819(A), 2103.D-5067(A), 105.20N7.001, 0104.D-0600(E), 103.202P.002; PIs: Levan, Tanvir). We retrieve the X-shooter images from the ESO archive facility and reduce r -band images using standard IRAF/ccdproc tasks. We use the fully reduced HAWK-I images from the ESO archive. We reduce the r -band MMT/BINOSPEC (Program 2019C-UAG199, UAO-G205-23B; PIs: Fong, Rastinejad) images using a custom Python pipeline⁵. For all bands, we utilize a template image obtained with the same instrument

at $\delta t \gtrsim 500$ days for HOTPANTS image subtractions. We calibrate our images using SDSS (r ; Alam et al. 2015) or 2MASS (JHK ; Skrutskie et al. 2006) stars in the field. Finally, where a residual at the position of the SN is detected at $> 3\sigma$ level, we perform aperture photometry with IRAF. We report all our observations in Table 2.

2.6. Assessing Transient Contamination in Template Images

Across all events, we consider the potential for afterglow or SN contamination in our *HST* template images, which may affect image subtraction residuals and bias our reported colors. Given that our sources are embedded in their host galaxies and likely to occur in star-forming regions (e.g., Blanchard et al. 2016; Lyman et al. 2017), thus making simple visual inspection difficult, we apply an analytic model to determine the expected magnitude of the SN or afterglow at the time of the template image.

As we will show in Section 3.2, for GRBs 030329, 100316D and 190829A we expect the SN to dominate at late times, while for GRB 130427A we expect the afterglow to be the main source of emission at the time of the template image (Figure 2). To assess the SN contribution for the former GRB-SNe, we fit a simple ^{56}Ni and ^{56}Co decay model (e.g., Arnett 1982; Tinianont et al. 2022; Kilpatrick et al. 2023) to the late-time ($\delta t \gtrsim 110$ days) optical (typically, the r , R , F606W and/or F555W bands) light curve. We then extrapolate the expected magnitude to the time of the template image. We find that the SN contribution in the template images ranges between $m = 27.8 - 30.7$ mag with the greatest potential contribution for GRB 100316D. However, as all of the GRB 100316D photometry is significantly brighter than this limit ($m \leq 24.6$ AB mag) we consider any template contribution negligible. To assess the afterglow contribution for GRB 130427A we extrapolate the afterglow decay to late times using the parameters described in Section 3.2, and predict any SN or afterglow contamination to be $m_{\text{F606W}} \gtrsim 28.6$ mag and $m_{\text{F160W}} \gtrsim 28.0$ mag. We note that this may indicate transient contamination that would impact later ($\delta t \gtrsim 300$ days) F160W observations. However, as we justify further in Section 3.2, we do not use these late-time color measurements to probe SN r -process enrichment as they are likely dominated by afterglow emission. Further, as our earlier ($\delta t \approx 22, 74$ days) SN-dominated observations of GRB 130427A are brighter than 23 mag, we do not expect contamination in the template to affect our SN colors.

⁵ <https://github.com/CIERA-Transients/POTPyRI>

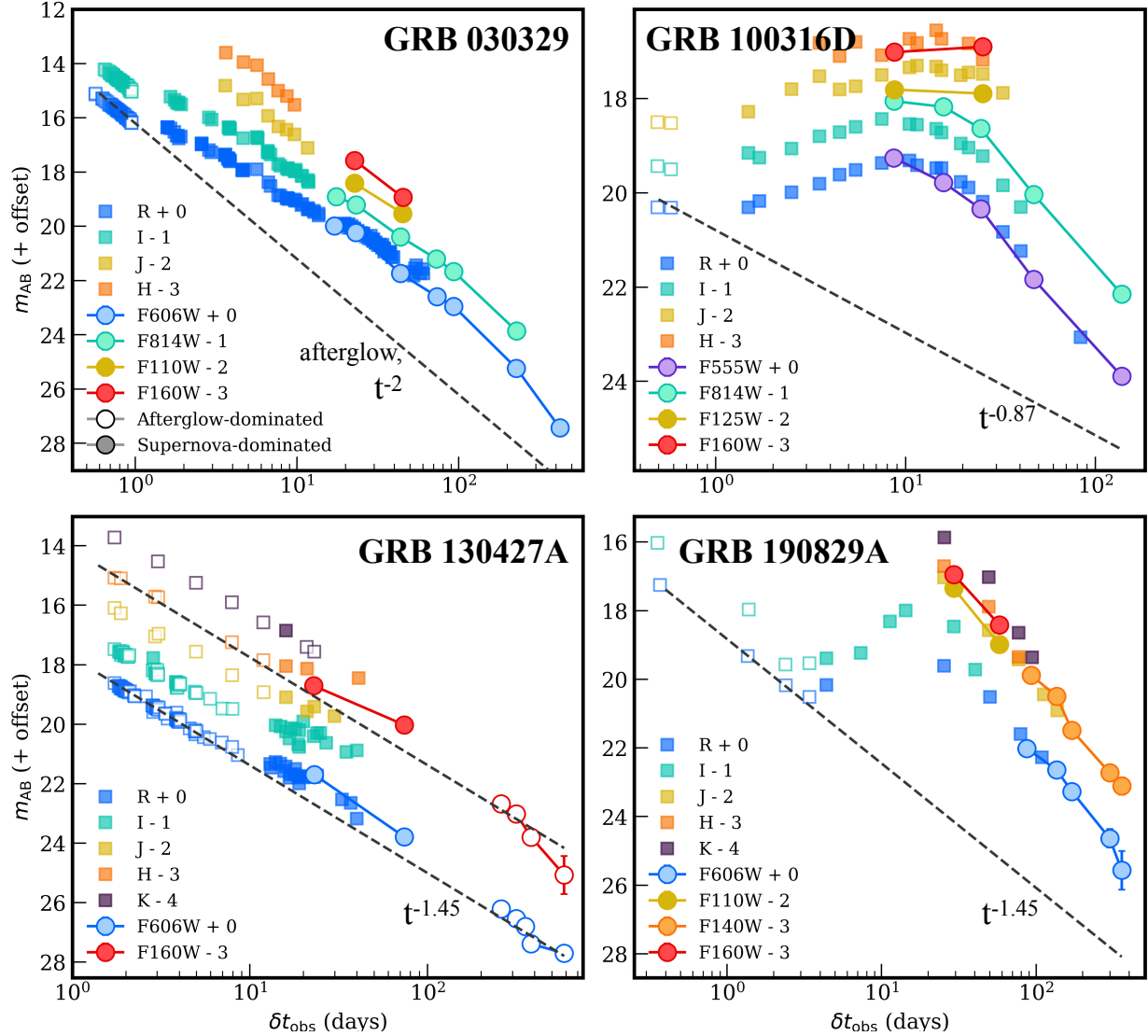


Figure 2. All data used in this work for GRBs 030329, 100316D, 130427A and 190829A in apparent magnitude (m_{AB}) versus observed time after the GRB triggers (δt_{obs}), corrected for Milky Way and local dust extinction. Ground-based observations are shown with squares while *HST* observations are represented with circles. In each panel we show the extrapolated r -band (and H -band for GRB 130427A) afterglow decay with a dashed line (further described in Section 3.2) and mark observations that are dominated or significantly (> 0.3 mag difference) contaminated by afterglow flux with open symbols. For instance, we expect that our *HST* observations of GRB 130427A observed beyond 200 days are contaminated or dominated by afterglow flux.

3. DETERMINATION OF THE INTRINSIC SUPERNOVA COLORS

3.1. Correcting for Line-of-Sight Dust Extinction

Dust extinction along the GRB’s line of sight may significantly contaminate the observed optical-NIR color of the SNe in our sample though, notably, it does not impact the relative color evolution. However, it is important to take into account because particularly high extinction may result in a reddened light curve that will affect any identification or constraints on r -process material. In addition to corrections for Galactic extinction, we correct for extinction from the local environment of

the GRB (Table 1), the assumptions of which we discuss below.

We utilize local or, when not available, host galaxy extinction values ($E(B-V)_{loc}$) from the literature (Matheson et al. 2003; Cano et al. 2011; Bufano et al. 2012; Levan et al. 2014a; Chand et al. 2020; Huang et al. 2023) and apply a Small Magellanic Cloud (SMC) extinction law (Cardelli et al. 1989; Gordon et al. 2003) to determine corrections in each filter. We employ the SMC extinction law as it is a well-studied dust relation for a stellar population with a higher specific star formation rate compared to the Milky Way, appropriate for long GRB host galaxies (Kann et al. 2006; Schady et al. 2012)

especially given that they have high star formation rates (e.g., Fruchter et al. 2006; Blanchard et al. 2016; Lyman et al. 2017). We note that the choice of extinction law will not significantly impact our optical-NIR corrections (as opposed to the ultraviolet regime).

For GRBs 030329, 100316D and 130427A, the derived values are low ($E(B - V)_{\text{loc}} < 0.15$ mag; Table 1) and where multiple values exist in the literature, they are consistent within ≈ 0.10 mag. For GRBs 100316D and 130427A, we take values of $E(B - V)_{\text{loc}}$ measured from spectroscopy of the afterglows covering the Na I D doublet ($\lambda\lambda 5890, 5896$) and calculated using a Milky Way gas-to-dust ratio (Table 1; e.g., Bufano et al. 2012; Xu et al. 2013). For GRB 130427A this value is consistent with $E(B - V)_{\text{loc}}$ calculated from the multi-wavelength afterglow spectrum (Perley et al. 2014). For GRB 030329 there is no measurement from afterglow spectroscopy or fitting, so we utilize a value derived from the $H\alpha/H\beta$ ratio in the host galaxy spectrum (Matheson et al. 2003). Literature values for local extinction of GRB 190829A are significantly higher. Using the XRT and *Swift*/Ultra-Violet Optical Telescope (UVOT) spectrum, Chand et al. (2020) derive $E(B - V)_{\text{loc}} = 1.04$. We note there is also a measurement $E(B - V)_{\text{loc}} = 0.64$ derived from the XRT light curve alone (Huang et al. 2023), but we prefer the value that incorporates UVOT data as this encompasses the regime where dust is most pronounced.

3.2. Characterizing the Afterglow Contribution

The GRB afterglow, typically modeled as synchrotron emission from the interaction of the jet with the surrounding medium, is expected to dominate over any SN emission in the few days following a burst (though this timescale may be highly variable). On week- to month-long timescales, SN emission typically dominates in the optical band given the afterglow’s steep power law decay (though there are notable exceptions in which the afterglow dominates for several months; e.g., GRB 221009A; Levan et al. 2023b). In the majority of cases, we expect that follow-up on timescales beyond a \sim month will probe the SN’s color evolution. In the majority of cases, we expect that follow-up on timescales beyond a \sim month will probe the SN’s color evolution. Therefore, the *HST* observations extending to very late times should be free from afterglow contamination. However, as using color evolution to determine *r*-process-enrichment in a GRB-SN is our primary objective, it is critical to determine which observations are clearly dominated by the SN emission.

Hence, we undertake a literature search to determine the temporal evolution ($F \propto t^\alpha$, where F is the observed

flux) for GRB afterglows to extrapolate as needed to the timescales of our observations. For GRB 030329 we utilize the post jet-break (observed at ≈ 0.5 day) afterglow decay of $\alpha = -2$ (Lipkin et al. 2004; Moss et al. 2023). We note that at early times this afterglow is complex and contaminated by flares (e.g., Lipkin et al. 2004; Tiengo et al. 2004; Kamble et al. 2009), but we expect its late-time behavior to decline smoothly. For GRB 100316D, the optical afterglow was faint compared to the SN even at early times, and we use the late-time X-ray temporal slope of $\alpha = -0.87$ (Margutti et al. 2013). For GRB 130427A we use $\alpha = -1.45$ measured from the multi-wavelength afterglow (Perley et al. 2014). We note that Maselli et al. (2014) observe a jet break in the X-ray and optical light curves at $\delta t \approx 10$ hours post-burst, followed by a decline of $\alpha = -1.36$. We prefer the values of Perley et al. (2014) which do not detect a jet break as their dataset includes greater temporal coverage (see also De Pasquale et al. 2016 who do not find evidence for a jet break in X-ray observations out to ~ 2.5 years). Finally, for GRB 190829A we utilize the *r*-band temporal index of $\alpha = -1.45$ from early GTC imaging (Hu et al. 2021). Apart from GRB 130427A, none of the GRBs in our sample have late-time jet breaks suggested in the literature.

We employ the above values for α and early observations to extrapolate the afterglow decay in each band and determine in which observations the predicted afterglow flux dominates our observations or is within 0.3 mag of the observed value. We plot the expected *r*-band afterglow contributions in Figure 2 as grey dashed lines. In Figure 2 and Table 2 we denote observations that are likely afterglow-dominated, which we ignore in the analysis that follows. We do not anticipate any significant afterglow contamination in the light curves of GRBs 030329, 100316D and 190829A past $\delta t \approx 4$ days. However, under our assumption of no observed jet break, the afterglow significantly contributes to or dominates the SN in the light curve of GRB 130427A at $\delta t \gtrsim 200$ days (Figure 2).

3.3. Supernova Dust Contribution

We briefly consider the possibility that dust produced by the SN may contribute to any observed reddening. The timescales for the production of dust in CC-SNe remain uncertain, though new observations with *JWST* are beginning to constrain the dust abundance in Type II SNe on \sim decade timescales (e.g., Hosseinzadeh et al. 2023; Shahbandeh et al. 2023). However, unlike these Type II SNe, our sample includes only relativistic, stripped-envelope GRB-SNe, as identified by the broad-lined features in their spectra. The mean ab-

sorption velocity measured for a large sample of GRB-SNe is $\sim 0.07c$ (Modjaz et al. 2016; see also Mazzali et al. 2021), indicating a high shock speed that would destroy any precursor dust grains before they may amass significantly. In addition, with the exception of a few rare cases, stripped-envelope SNe like GRB-SNe are rarely observed to have significant circumstellar material (CSM), making any contribution from pre-existing dust unlikely (e.g., Prentice et al. 2019; Szalai et al. 2021). On the $\lesssim 3$ year timescales of our observations we conclude that SN-produced dust will not significantly contribute to our SN colors.

4. EXPLORING R -PROCESS ENRICHMENT IN OUR OBSERVATIONAL SAMPLE

4.1. Direct Comparison of the Sample to Models

We compare our extinction-corrected SN observations to the semi-analytic radiation transport models of Barnes & Metzger (2022) for a collapsar SN enriched with r -process material. In this collapsar r -process scenario, weak interactions within the dense and hot accretion disk feeding the black hole favor neutronization of the disk material (above a critical accretion rate $\sim 10^{-3} - 10^{-2} M_{\odot} \text{ s}^{-1}$; De & Siegel 2021). A fraction of this neutron-rich midplane material is then ejected in disk winds, which undergoes r -process nucleosynthesis in the outflow on large scales. This process is similar to the disk outflows which contribute significantly to r -process production and kilonova emission in neutron star mergers (Siegel et al. 2019; Barnes & Metzger 2022). However, unlike in a merger, these r -process disk wind ejecta collide with and subsequently mix with the outer (non- r -process enriched) layers of the SN. The degree and radial extent of this mixing are uncertain and may be enhanced in the presence of a jet, resulting in a viewing angle dependence (Barnes & Duffell 2023).

Barnes & Metzger (2022) predict that r -process material mixed with typical SN Ic-BL ejecta will produce a distinguishable red photometric color (distinct from the natural blue to red evolution of r -process-free models) that becomes pronounced on timescales of a few weeks to months. Naturally, larger dynamic ranges in filters hold larger discriminating power between models. The existing suite of models assumes a spherical distribution of ejecta parameterized by total SN ejecta mass (M_{tot}), ^{56}Ni ejecta mass ($M_{56\text{Ni}}$), average ejecta expansion velocity as a fraction of the speed of light (β_{ej}), mass of r -process material (M_{rp}) and the mixing coordinate (ψ_{mix}). ψ_{mix} describes the radial extent out through the SN ejecta to which the r -process enriched layers are mixed. Values of ψ_{mix} closer to 1 indicate a greater degree of radial mixing (the limit $\psi_{\text{mix}} = 1$ cor-

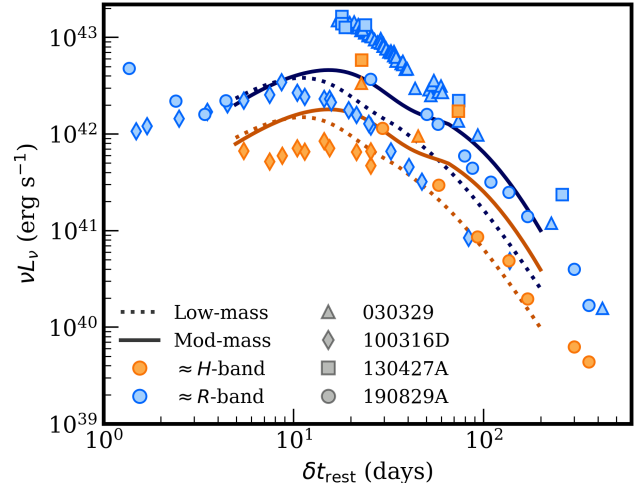


Figure 3. R - (blue) and H -band (orange) models of Barnes & Metzger (2022) for r -process-enriched SNe Ic-BL (lines) overlaid with our sample of rest-frame, Galactic and local extinction-corrected observations. We show only observations that are SN-dominated (Section 3.2). We plot fiducial r -process-free low-mass (dotted; $M_{\text{ej}} = 1.51$, $M_{56\text{Ni}} = 0.21$, $\beta_{\text{ej}} = 0.05$) and moderate mass (solid; $M_{\text{ej}} = 3.97$, $M_{56\text{Ni}} = 0.33$, $\beta_{\text{ej}} = 0.02$) SNe Ic-BL models and compare against observations of GRBs 030329, 100316D, 130427A and 190829A (Section 4). We emphasize that these are not fits, but instead are meant to be instructive in determining the family of models to use for comparison to each GRB-SN. By eye, we determine that the light curves GRBs 100316D and 190829A are most compatible with the low-mass model, while GRBs 030329 and 130427A are compatible with the moderate-mass model. We utilize these fiducial comparisons throughout the rest of our analysis.

responds to the r -process material being homogeneously mixed all the way to the ejecta surface), resulting in a more pronounced and prolonged red color (Figure 4).

Given the large uncertainties in GRB-SNe parameter inference (Cano et al. 2017a,b; Hu et al. 2021), we constrain the number of free parameters (so we are left with only M_{rp} and ψ_{mix}) by comparing our observational catalog to the most compatible fiducial collapsar model of Barnes & Metzger (2022) using visual inspection. We employ the fiducial models for low-, moderate- and high-mass collapsar SNe from Barnes & Metzger (2022) which are parameterized by $M_{\text{ej}} = 1.51, 3.97$ and $10.45 M_{\odot}$, $M_{56\text{Ni}} = 0.21, 0.33$ and $0.85 M_{\odot}$, and $\beta_{\text{ej}} = 0.05, 0.02$ and $0.03c$, respectively. In Figure 3 we compare our r - and H -band luminosities to the low-, moderate-, and high-mass models (but do not show the high-mass model as it does not provide a reasonable visual match to any of the GRB-SNe). From visual inspection, we determine that GRBs 100316D and 190829A are comparable to the

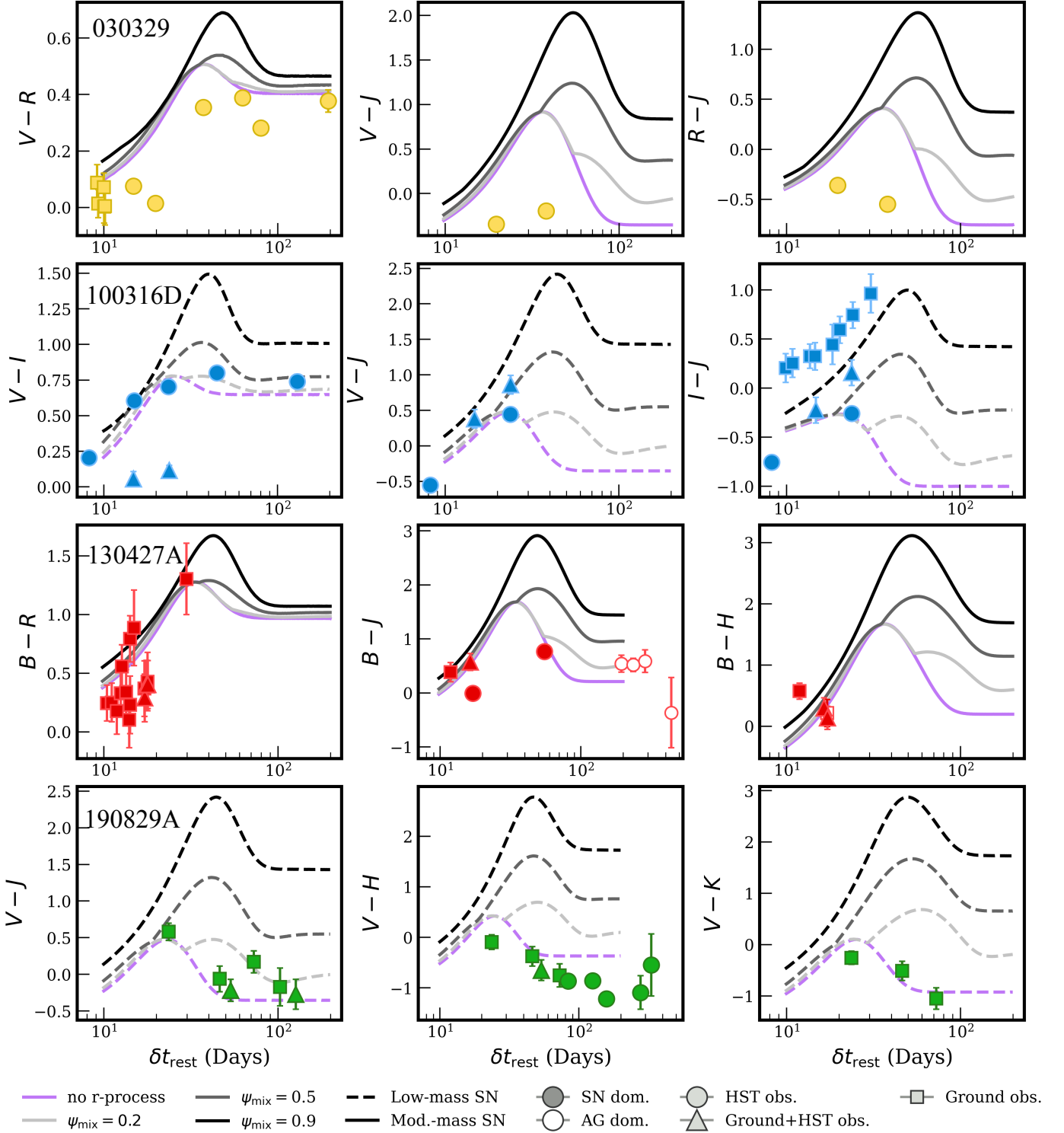


Figure 4. Assorted colors of the four GRB-SNe in our sample versus rest-frame time compared to models from Barnes & Metzger (2022) with fixed r -process mass ($M_{\text{rp}} = 0.03$) and varying values of ψ_{mix} (lines). We also plot models without r -process enrichment in purple. Afterglow-dominated observations are shown as open symbols, and measurements dominated by SN are filled symbols. Low-mass (dashed lines) SN Ic-BL color evolution models are shown against observations of GRBs 100316D and 190829A and while moderate-mass (solid) models are shown against colors of GRBs 030329 and 130427A (Barnes & Metzger 2022; Figure 3) based on our analysis in Section 4. GRBs 030329 and 190829A are, at some epochs, bluer than the models and do not show strong evidence for r -process enrichment with a high degree of mixing. The $V - I$ colors of GRB 100316D favor enrichment at a moderate mixing fraction. The optical-NIR colors of GRBs 100316D and 130427A are consistent with both r -process-free models and those for higher values of ψ_{mix} and r -process enrichment.

low-mass model, while GRBs 030329 and 130427A are comparable to the moderate-mass model.

We next plot these models against our observations in color space to determine if any GRB-SNe in our sample show evidence for r -process enrichment. Each of these fiducial models is enriched with $M_{\text{rp}} = 0.03M_{\odot}$, a moderate value consistent with theoretical yields (e.g., Siegel et al. 2019). In Figure 4 we show the three best-sampled colors for each burst. We calculate colors for observations taken within three days of each other across ground- and space-based facilities. For windows beyond three days, the models predict changes in color will be greater (Figure 4). Models are available in the $UBVRIJHK$ -bands, so we compare our observations to the nearest approximate rest-frame model band and correct for time dilation using the redshift of the GRB (Table 1). We explore how the GRB-SN color evolution compares to models as a function of mixing fraction, and also compare to an r -process free model.

For GRB 030329, the latest observed colors are rest-frame $V - R$, where model color differences are small between the r -process-free and enriched cases. GRB 030329’s optical-NIR colors are $\gtrsim 0.5$ mag bluer compared to the models, including the r -process-free model. Overall, we find that this GRB-SN provides a poor fit to the models.

For GRB 100316D, our rest-frame $V - I$ high signal-to-noise observations are consistent with r -process-enriched models, but not the unenriched case. On the other hand, our optical-NIR observations of GRB 100316D appear to favor lower values of ψ_{mix} or r -process-free models, though we note that ground-based colors favor high ψ_{mix} models. We ascribe the difference between ground-based and *HST* rest-frame $I - J$ to discrepancies between the GROND i and *HST* F814W light curve (Figure 2; Table 2). Later NIR observations of this burst would be necessary in determining if the optical-NIR colors are consistent with the preference for enrichment found by the rest-frame $V - I$ colors.

In GRB 130427A, the uncertainties of rest-frame ground-based $B - R$ data are too large to distinguish between even strong mixing or r -process-free models. Optical-NIR color measurements are consistent with both models for enrichment with low ψ_{mix} or models for no enrichment. Unfortunately, observations at $\gtrsim 180$ days are likely contaminated by the afterglow and are thus not used in this analysis (Section 3.2; Figure 2).

Finally, the $V - J$ colors of GRB 190829A are reasonably matched to both the r -process-free and low ψ_{mix} models. However, later $V - H$ and $V - K$ colors are more consistent with the r -process free model and are

distinct from the enriched $\psi_{\text{mix}} = 0.2$ model by up to ~ 1 mag.

In general, we find that with a few exceptions, observations of GRBs 030329, 100316D and 130427A are consistent with $\psi_{\text{mix}} \lesssim 0.5$ for $M_{\text{rp}} = 0.03M_{\odot}$ (Figure 4), though inference between filters may vary. Most of these GRBs’ color measurements are not on sufficient timescales to distinguish between r -process-free and low ψ_{mix} values. On the other hand, the well-sampled color measurements of GRB 190829A provide a strong case for no r -process enrichment at the level of the models used in this section ($M_{\text{rp}} = 0.03M_{\odot}$). Future color measurements with the cadence and long baseline similar to GRB 190829A would allow for more detailed population studies.

4.2. Observed Color Diversity Amongst GRB-SNe Sample

Already, we observe diversity in color evolution within our sample of 4 GRB-SNe. In Figure 5 we plot SN-dominated color measurements for each GRB that are most closely matched to the $V - H$ filters (chosen due to late-time data availability). While for GRBs 030329, 100316D and 190829A the rest-frame filters are reasonably comparable, the higher redshift of GRB 130427A results in bluer rest-frame filters ($\approx B - J$) for the data plotted. We note that this difference in low- and high-redshift rest-frame bands may produce color differences up to ≈ 0.5 mag (based on Barnes & Metzger 2022 models).

Figure 5 highlights the diversity within the GRB-SNe sample in terms of their color evolution. At $20 \lesssim \delta t \lesssim 60$ days GRB 100316D’s SN is reddening rapidly, GRB 030329’s SN is more slowly reddening, and GRB 190829A’s SN is becoming bluer (Figure 5). This behavior may be explained by differences in M_{ej} or V_{ej} , or perhaps M_{rp} or ψ_{mix} between the GRBs.

In Figure 5 we also compare the GRB-SNe to the large SNe Ic-BL compilation of Anand et al. (2023). This sample includes color measurements for 25 nearby SNe Ic-BL, none of which show strong evidence for r -process enrichment when fit to models. Observations from this sample are corrected for Galactic extinction but not local extinction, though none of their SNe spectra indicate strong local dust. In general, the color evolution of the GRB-SNe in our sample is consistent with those of the Anand et al. (2023) sample, indicating there is no difference in $R - H$ color evolution and observed diversity between SNe Ic-BL discovered with and without GRB counterparts. This observed trend contrasts with theoretical expectations that GRB-SNe are more likely to produce larger M_{rp} and ψ_{mix} (and thus more pro-

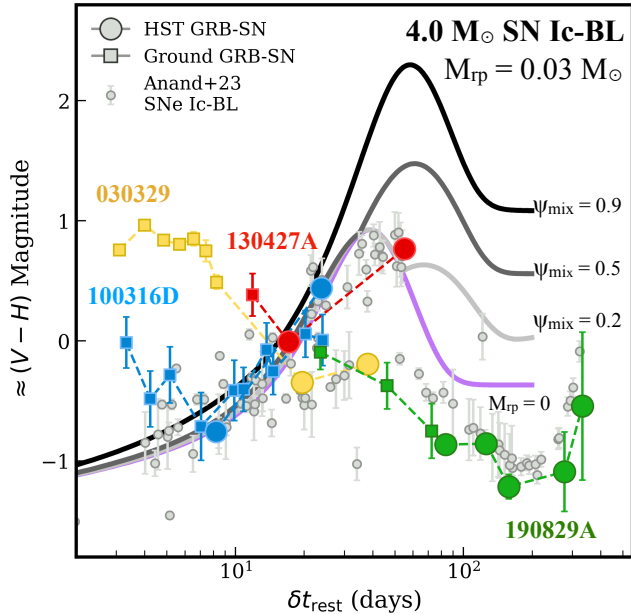


Figure 5. The approximate rest-frame $V - H$ color evolution of SN-dominated observations of GRB 030329 (yellow), GRB 100316D (blue), GRB 130427A (red), and GRB 190829A (green), corrected for Galactic and local extinction. Ground-based observations are shown with squares, while observations obtained with *HST* are represented with circles, and extend the majority of the color evolution curves significantly. Against these observations we plot color evolution models for a moderate-mass SN Ic-BL enriched with $0.03 M_{\odot}$ r -process material (greyscaled; color gradient corresponding to ψ_{mix}) or r -process-free (purple; Barnes & Metzger 2022). Broadly, the observations are consistent with both models free of r -process material and those with low mixing fractions. There is $\gtrsim 1$ magnitude of diversity in the color evolution of the bursts in our sample between $20 \lesssim \delta t \lesssim 80$ days.

nounced red colors; Siegel et al. 2019; Barnes & Duffell 2023) due to their high angular momentum and accretion disk sizes. Rather, we do not find evidence for differences in color evolution between GRB-SNe and SNe Ic-BL observed without jets.

4.3. Quantitative Constraints on M_{rp} and ψ_{mix}

We next consider a larger range of M_{rp} values and constrain the M_{rp} and ψ_{mix} for each GRB-SN. To do this, we employ large grids of fiducial models parameterized by combinations of these two parameters (Barnes & Metzger 2022). We employ the same low- and moderate-mass fiducial parameters for GRBs 100316D, 190829A and GRBs 030329 and 130427A as in Section 4 (e.g., Figure 3) and hold these constant across the grid. The grids are linearly spaced in ψ_{mix} between 0.1 and 0.9, and at fixed values, $M_{\text{rp}} = 0.01, 0.03, 0.08$ and $0.15 M_{\odot}$ (Barnes & Metzger 2022). We consider only observa-

tions taken between $20 < \delta t < 200 \times (1 + z_{\text{GRB}})$ days as the color differences on early timescales are negligible between models. For each color observation, we determine the $M_{\text{rp}}-\psi_{\text{mix}}$ pairs whose predicted model colors are consistent within the observed 3σ color errors. To account for *HST* systematic errors, where the 3σ error is < 0.1 mag, we use a threshold of 0.1 mag to find consistent models.

In Figure 6 we show the $M_{\text{rp}}-\psi_{\text{mix}}$ parameter space. We color code and label each cell according to the percentage of observations that are consistent with the model parameterized by the corresponding $M_{\text{rp}}-\psi_{\text{mix}}$ pair. White space indicates that models for that $M_{\text{rp}}-\psi_{\text{mix}}$ pair are not consistent with observed colors. In general, the reason observations are inconsistent is owed to their bluer colors compared to the models (Figure 4).

For GRB 030329, we find that, unsurprisingly given that the colors are significantly bluer than those in the comparison models (Figure 4), only two observations are consistent with the colors of the grid. These observations favor $\psi_{\text{mix}} \lesssim 0.4$ but do not provide strong constraints on M_{rp} . For GRB 100316D we find that twelve color observations ($\approx 71\%$) are most consistent with some part of the explored parameter space. These observations are consistent with models for a combination of $\psi_{\text{mix}} \lesssim 0.4$ and $M_{\text{rp}} = 0.03 - 0.15 M_{\odot}$. For GRB 130427A our colors do not have strong constraining power but favor lower values for both parameters, though high values for M_{rp} and ψ_{mix} are each allowed if in tandem with a low value for the other parameter. Finally, for GRB 190829A our constraints are consistent with our findings in Section 4, the majority of color observations of GRB 190829A are consistent with low values for ψ_{mix} . The model for which the greatest percentage of observations (56%) is consistent is parameterized by $M_{\text{rp}} = 0.01 M_{\odot}$ and $\psi_{\text{mix}} = 0.1$. All observations of GRB 190829A that are not consistent with the grid are bluer than the observed colors.

Finally, we combine each GRB's grid from Figure 6 to search for trends across the population. In Figure 7 we show the average percentage of observations consistent with each $M_{\text{rp}}-\psi_{\text{mix}}$ pair across the four GRBs. We also show histograms for each parameter that denote the normalized percentage of observations that are consistent with each parameter pairing. The pairs that are consistent with the greatest percentage of observations are all for values of $\psi_{\text{mix}} = 0.1$ and span $0.01 \leq M_{\text{rp}}/M_{\odot} \leq 0.08$. We observe a drop in percentage of consistent observations between models for $\psi_{\text{mix}} = 0.4$ and $\psi_{\text{mix}} = 0.5$, indicating that models for $\psi_{\text{mix}} \leq 0.4$ are preferred for our sample of GRB-SNe. We do not find strong constraints on M_{rp} across ψ_{mix}

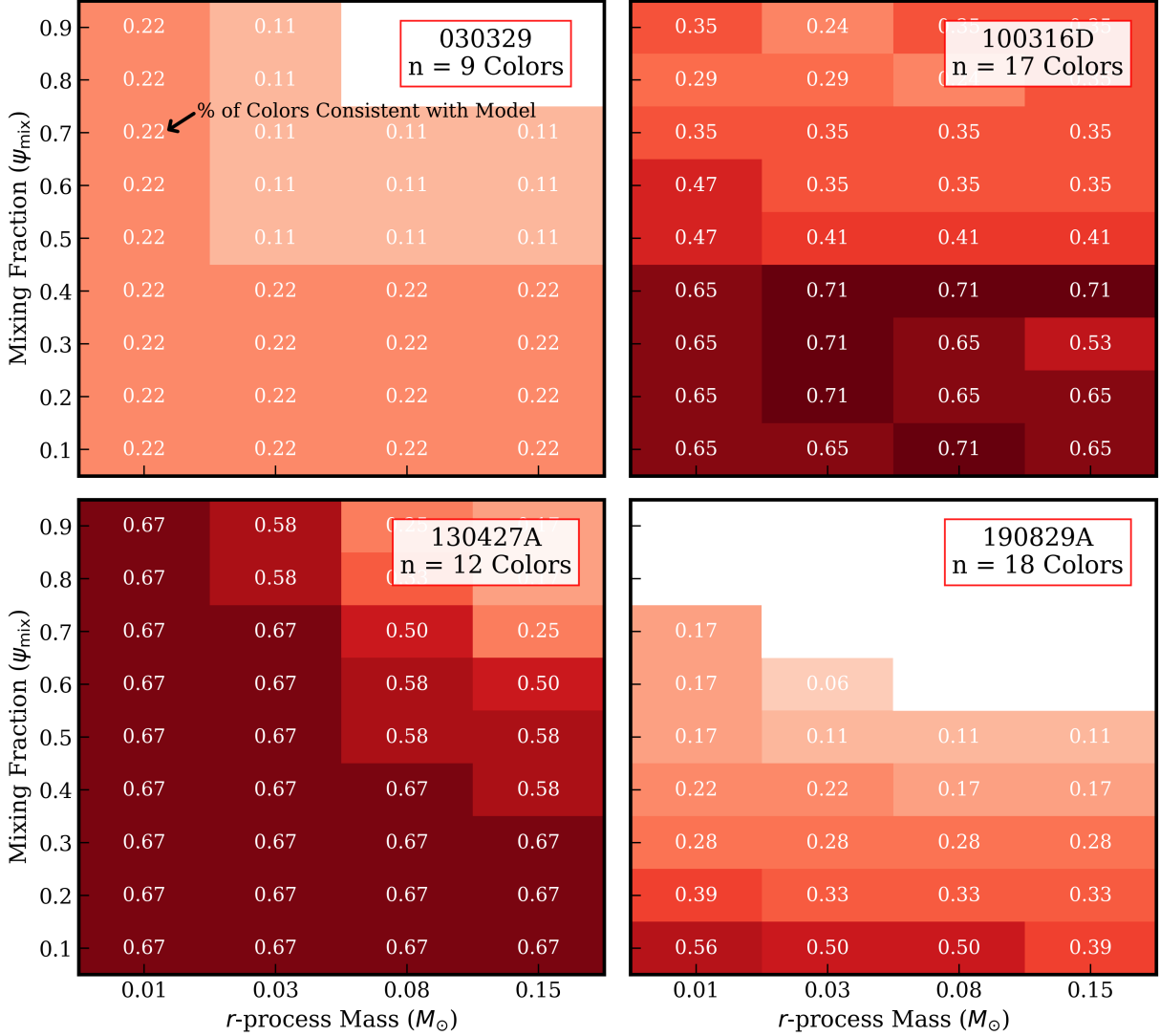


Figure 6. Comparison of our observational catalog to a large grid of models for a range of r -process masses and mixing fractions. Each cell in the grid represents a model from [Barnes & Metzger \(2022\)](#) parameterized by the corresponding M_{rp} and ψ_{mix} . The color shade and labeled number of each cell corresponds to the percentage of color observations consistent within 3σ of the model parameterized by that combination of M_{rp} and ψ_{mix} out of the total (labeled ‘n’) color observations per GRB meeting our criteria. Observations of GRBs 030329 and 130427A do not strongly constrain M_{rp} and ψ_{mix} , though they generally favor lower values. Observations of GRB 190829A are highly consistent with $\psi_{\text{mix}} \lesssim 0.1$ and favor lower values of M_{rp} . In contrast, observations of GRB 100316D are consistent with the full range of $0.01 \leq M_{\text{rp}}/M_{\odot} \leq 0.15$ and $\psi_{\text{mix}} \lesssim 0.4$.

values from our observations, although observations may slightly favor values for $M_{\text{rp}} \leq 0.03M_{\odot}$ (Figure 7).

5. DISCUSSION

5.1. Connection Between ψ_{mix} , γ -ray and SN Properties

We consider any potential connections between the γ -ray, SN and r -process enrichment properties and compare them against theoretical predictions from the literature. From 2D hydrodynamical simulations, [Barnes & Duffell \(2023\)](#) propose that GRBs with the longest rest-frame γ -ray durations will be accompanied by SNe

with higher ψ_{mix} values, as both properties are correlated with a long-lived, more massive disk wind. In addition, they find that a higher initial SN explosion energy is associated with lower values of ψ_{mix} .

In Section 4, we concluded that, within the sample, GRB 100316D observations are highly consistent with mixing values up to $\psi_{\text{mix}} = 0.4$ while the observed colors of GRB 190829A prefer $\psi_{\text{mix}} \lesssim 0.2$ (Figure 6). For GRBs 030329 and 130427A observations favored lower values of ψ_{mix} , but higher values were allowed in combination with $M_{\text{rp}} = 0.01M_{\odot}$ (Figure 6). Comparing the results of GRBs 100316D and 190829A to the T_{90}

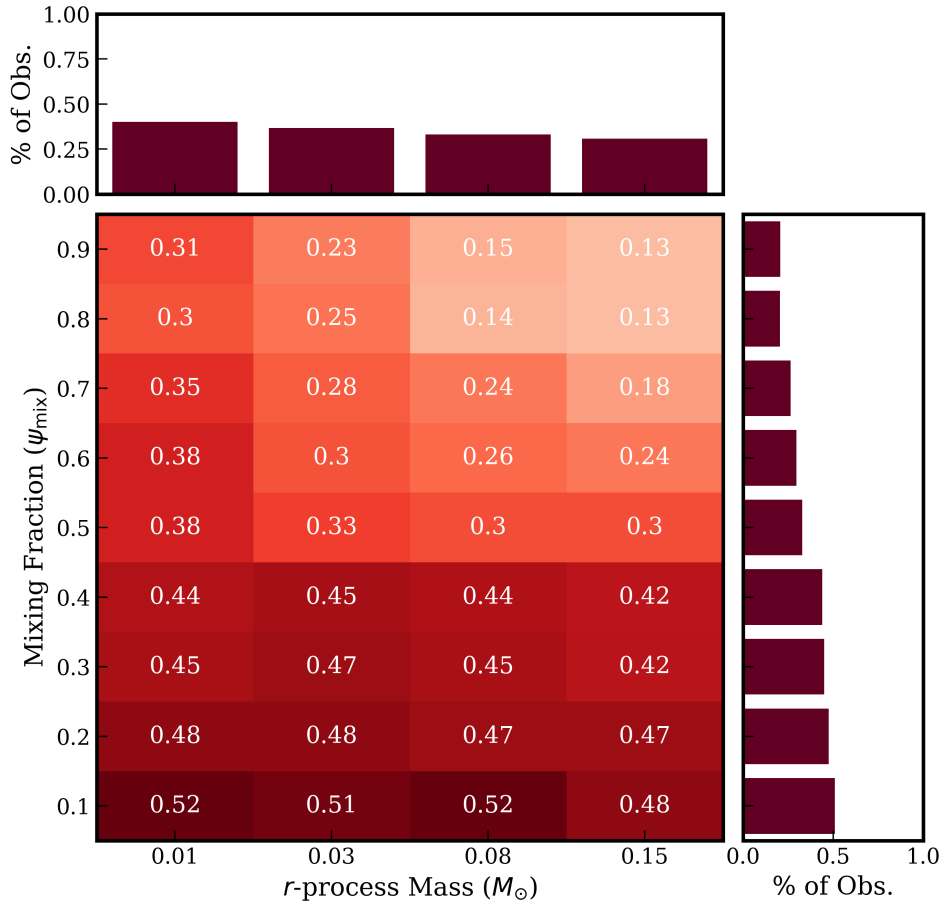


Figure 7. $M_{\text{rp}}-\psi_{\text{mix}}$ constraints across the four GRBs in our sample that are shown in Figure 6. In the central panel, the color shade and labeled white number denotes the percentage of observations, averaged across the four GRB-SNe, that are consistent with the corresponding $M_{\text{rp}}-\psi_{\text{mix}}$ pair. Histograms along the M_{rp} and ψ_{mix} axes show the percentage of consistent observations and demonstrate a decrease in consistency around $\psi_{\text{mix}} \approx 0.4$, indicating that most observations favor these lower mixing fractions. Our observations are not very constraining of M_{rp} but may favor lower values.

rest-frame γ -ray durations listed in Table 1 and literature values of the SN explosion energy (e.g., Cano et al. 2017a,b; Hu et al. 2021), we explore trends in our sample. GRB 100316D (for which observations are consistent with $\psi_{\text{mix}} \approx 0.4$) has the longest rest-frame T_{90} γ -ray duration (a lower limit of 261 s as seen by *Swift*) and the lowest SN explosion energy (Cano et al. 2017a) in our sample. We note that this GRB belongs to the low-luminosity class, which may be indicative of a less energetic central engine or shock breakout. GRB 190829A (for which we deduce $\psi_{\text{mix}} \leq 0.1$) has a shorter γ -ray duration (rest-frame 49 s as seen by *Swift*) and a higher estimated SN explosion energy (Hu et al. 2021). Though these are just two examples, they align with the trends predicted by Barnes & Duffell (2023). An expansion of $M_{\text{rp}}-\psi_{\text{mix}}$ constraints for GRB-SNe is necessary to determine if these trends hold within a statistically significant sample.

The findings of Barnes & Duffell (2023) suggest that ultra-long GRBs (ULGRBs; Levan et al. 2014b) may

be the ideal candidates for production of r -process elements.⁶ We consider but ultimately do not include several ULGRBs in our sample due to their high redshifts ($z \gtrsim 0.6$; e.g., Levan et al. 2014b; Greiner et al. 2015) or an absence of confirmed SN counterpart (e.g., GRB 130925A; Evans et al. 2014; Piro et al. 2014). However, these factors may also limit future rates of nearby ULGRBs suitable for deep NIR follow-up.

5.2. Universal r -Process Enrichment Implications

As an exercise, we use our constraints to infer an average r -process mass from GRB-SNe, quantify the contribution of these events to the Universe’s r -process budget, and compare our estimate to the Milky Way r -process enrichment. We caution that these results are

⁶ On the other hand, if the accretion rate onto the black hole is too low, the disk may not neutronize in the first place (e.g., Siegel et al. 2019; De & Siegel 2021), precluding the production of r -process elements.

highly model dependent and there are high uncertainties in these constraints. For this exercise, we separately consider the derived yields of $M_{\text{rp}} \leq 0.01M_{\odot}$ for GRB 190829A and $M_{\text{rp}} \approx 0.03 - 0.15M_{\odot}$ for GRB 100316D. These two GRBs are the only ones with constraints in our sample and while a range of r -process yields are expected, the median is unknown at this time (Siegel et al. 2019; Barnes & Metzger 2022). Specifically, we employ a yield of $M_{\text{rp}} = 0.07M_{\odot}$ for GRB 100316D (found using the average of the values consistent with the greatest fraction of observations; Figure 6) and $M_{\text{rp}} = 0.01M_{\odot}$, an optimistic value, for GRB 190829A.

We modify the equation of Rosswog et al. (2018) for events that produce r -process to determine the Milky Way contribution:

$$M_r \sim 17\,000M_{\odot} \left[\frac{\mathcal{R}_{\text{rp}}}{500\text{Gpc}^{-3}\text{yr}^{-1}} \right] \left[\frac{\bar{m}_{\text{ej}}}{0.03M_{\odot}} \right] \left[\frac{\tau_{\text{gal}}}{1.3 \times 10^{10}\text{yr}} \right] \quad (1)$$

where \mathcal{R}_{rp} is the event rate, \bar{m}_{ej} is the average r -process ejecta per event, and τ_{gal} is the Milky Way age. We fix $\tau_{\text{gal}} = 1.3 \times 10^{10}$ yr for all calculations. We first consider the case in which only CCSNe associated with long-duration GRBs (LGRBs) produce r -process such that $\mathcal{R}_{\text{rp}} = \mathcal{R}_{\text{LGRB}}(z=0) = 79_{-33}^{+57}$ Gpc $^{-3}$ yr $^{-1}$ (Ghirlanda & Salvaterra 2022). This rate is modeled using the distributions of observed parameters such as fluence, T_{90} , and jet opening angle from *Fermi*, the *Compton Gamma Ray Observatory* and *Swift* (Ghirlanda et al. 2007; Ghirlanda & Salvaterra 2022). For a GRB 100316D (GRB 190829A) yield this results in a total contribution of $M_r \sim 6300_{-2600}^{+4500}M_{\odot}$ ($900_{-370}^{+650}M_{\odot}$). This is significantly below the calculated total r -process of the Milky Way of $M_{\text{r,MW}} \approx 23\,000M_{\odot}$ (elements of nucleon number $A \geq 69$; Hotokezaka et al. 2018 measured from Europium abundances of local stars from Venn et al. 2004; Battistini & Bensby 2016). We note that other works find the total $M_{\text{r,MW}}$ may vary by several thousand M_{\odot} (e.g., Bauswein et al. 2014; Rosswog et al. 2018). However, taking $M_{\text{r,MW}} = 23\,000M_{\odot}$ and considering the yields of both GRBs 100316D and 190829A, we determine that GRB-SNe produce 2 – 47% of the Milky Way’s r -process abundance. If only GRB-SNe produce r -process amongst CCSNe, either their average M_{rp} yields must be significantly higher than what we derive for GRB 100316D and GRB 190829A, the rates of GRB-SNe are higher than used in our estimate (indeed, the LGRB rate of Ghirlanda & Salvaterra 2022 is based on bright GRBs and the rate of low-luminosity GRBs such as GRB 100316D may be higher) or GRB-SNe are a subdominant r -process production channel compared to BNS mergers.

As our above analysis indicates that GRB-SNe alone cannot account for $M_{\text{r,MW}}$, we consider the case in which collapsars, identified by SN Ic-BL alone, synthesize r -process elements. From the ZTF Bright Transient Survey, the total CCSNe rate is $(10.1_{-3.5}^{+5.0}) \times 10^4$ Gpc $^{-3}$ yr $^{-1}$ of which SNe Ic-BL represent $\approx 4\%$ (Percy et al. 2020). Combined, this results in a rate $\mathcal{R}_{\text{rp}} = \mathcal{R}_{\text{Ic-BL}}(z=0) = 3\,030$ Gpc $^{-3}$ yr $^{-1}$. Combined with our yield estimates for GRB 100316D (GRB 190829A), this gives $M_r \sim 240\,000M_{\odot}$ ($34\,000M_{\odot}$). Both of these rates overpredict Milky Way r -process enrichment. Thus, either only a fraction of SNe Ic-BL without GRBs produce r -process, or they are not a significant contributor, deduced from the significant mismatch in total r -process mass. This finding is consistent with the analysis of Anand et al. (2023).

Our above calculations are dependent on model assumptions of r -process observables in GRB-SNe. Notably, the abundance pattern of elements produced by CCSNe are highly uncertain which likely affects the observed spectral energy distribution (SED) and, thus, the resulting model colors. On the modeling side, abundances depend on observationally unconstrained parameters such as the black hole accretion rate in the collapsar scenario. Typical CCSNe are not expected to produce the heaviest r -process elements (but may produce up to the first peak; e.g., Wang & Burrows 2023) while collapsars may produce up to the third peak elements under high accretion rates or strong magnetic fields (but may still struggle to produce actinides; Siegel et al. 2019). We note that the models used in our analysis assume a r -process SED based on the kilonova AT2017gfo, which likely produced up to and beyond the lanthanide elements ($A \geq 140$; e.g., Kasen et al. 2017). Future models that account for mixing of only lighter r -process elements combined with *JWST* NIR spectroscopy (see Section 5.3) may help to identify and delineate the abundance pattern. Notably, unlike BNS mergers, long GRBs are localized to galaxies with young ages and high specific star formation rates. These locations lend themselves to enriching early generations of stars, especially compared to BNS mergers which more frequently occur on the outskirts of galaxies (Fong et al. 2022; Mandhai et al. 2022; O’Connor et al. 2022; van de Voort et al. 2022).

Our above derived rates are ballpark estimates and would benefit from additional modeling of r -process enriched collapsar light curves. Further modeling of r -process-enriched MR SNe light curves could also provide benchmarks for assessing heavy element production through a second mechanism. Similar to BNS mergers and kilonovae (e.g., Bauswein et al. 2014; Shen et al.

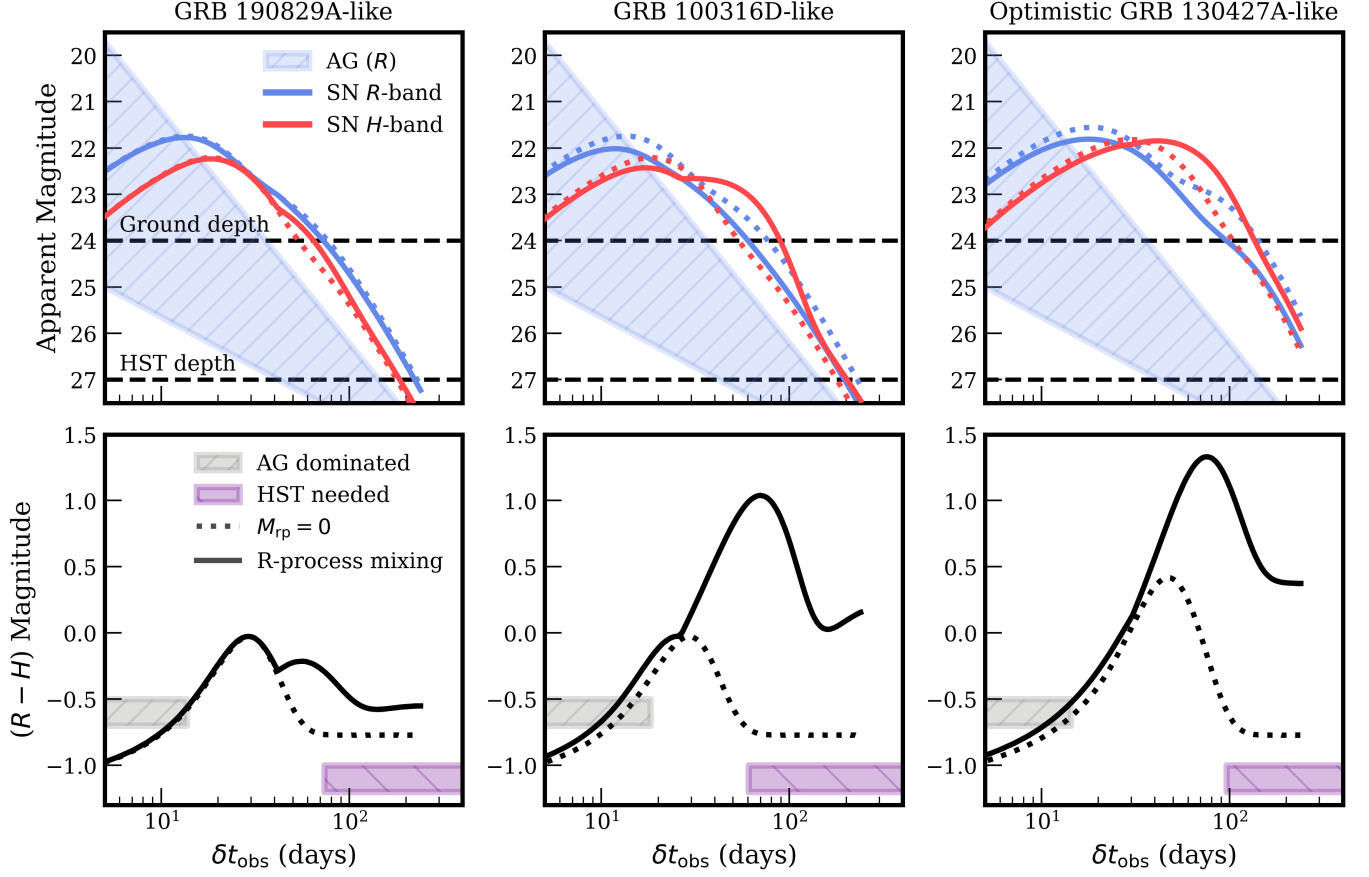


Figure 8. *Top:* expected R - and H -band light curves of a SN Ic-BL that is r -process-free (dotted lines) and enriched with r -process material (solid lines) set at $z = 0.2$ (Barnes & Metzger 2022). We show the expected afterglow brightness at $z = 0.2$ and the depths of large ground and space-based facilities at which $\approx 5\sigma$ detections should be possible (more details in Section 5.3). We show three models based on expected or potential outcomes of our analysis in Section 4: our favored parameters for GRB 190829A (left), our favored parameters for GRB 100316D (middle) and an observationally optimistic model that is consistent with observations of GRB 130427A (right). In the bottom panel, we plot $R - H$ over time for corresponding models, shading in grey the timespans at which the afterglow may dominate and in purple the timescales at which HST is necessary. To distinguish and monitor the color evolution of GRB 190829A-like and GRB 100316D-like models from the r -process-free case, space-based observations on the timescales of ~ 60 days are required. A SN Ic-BL like the optimistic GRB 130427A-like case would be distinguishable by large-aperture ground-based observatories.

2015; Rosswog et al. 2018; Hotokezaka et al. 2018 and references therein), our deduced M_r values will be improved with more constrained rate estimates and characterization of the observed diversity of GRB-SNe r -process yields.

5.3. Future Observations

The observational sample presented in this work was not fine-tuned for comparison to the recent models of Barnes & Metzger (2022). Here, we consider if and how future observational strategies of GRB-SNe can be designed to best observe and constrain M_{rp} and ψ_{mix} . In Figure 8 we consider the observability of models that were most consistent with our light curves of GRBs 100316D (low mass; $M_{rp} = 0.08M_{\odot}$, $\psi_{mix} = 0.4$) and 190829A (low mass; $M_{rp} = 0.01M_{\odot}$, $\psi_{mix} = 0.1$;

Section 4) in terms of both luminosity and color evolution, scaled to $z = 0.2$. In addition, we examine an optimistic (but consistent with observational constraints) case for GRB 130427A (moderate mass; $M_{rp} = 0.03M_{\odot}$, $\psi_{mix} = 0.7$; e.g., Figure 6). We also plot our r -band afterglow extrapolations of GRBs 030329, 100316D and 190829A shifted to $z = 0.2$ (spanning $m_r \approx 21 - 26$ AB mag at $\delta t \approx 1$ day; Section 3.2 and Figure 4) to understand how significantly this component will contaminate future low-redshift GRB-SNe at all times. We do not include GRB 130427A’s afterglow in the range as it was known to be superlative in its brightness (e.g., Perley et al. 2014; Laskar et al. 2013). In considering the sensitivity of large-aperture ground-based telescopes, we account for the fact that most GRB-SNe are embedded

in their host galaxies, thus requiring image subtraction which reduces the source’s signal-to-noise.

From Figure 8 we show that for a typical afterglow, we do not expect significant contamination on the timescales of the models ($\delta t \lesssim 300$ days). Our GRB 190829A-like model demonstrates that, to observe a similar event, *HST* sensitivity is necessary to distinguish the r -process-free and enriched cases ($R - H \lesssim 0.5$ mag). For the optimistic GRB 130427A-like case at $z = 0.2$, the SN color evolution could be fully monitored and distinguished using large-aperture ground-based telescopes. Overall, we find a wide diversity in expected luminosity and color evolution, but find that both ground- and space-based facilities can play an important role. Moreover, a large dynamic range in color is extremely useful to confirm r -process enrichment, and subsequently constrain models. As discussed in Section 4, an observational cadence similar to that of GRB 190829A is critical to constraining the r -process enrichment.

Beyond photometric searches, spectroscopy of GRB-SNe may definitively identify or place deep limits on observed emission lines from transitions of r -process elements. Spectroscopic observations of kilonovae have identified emission lines from individual elements, most notably Sr II ($\lambda 10500$; e.g., Watson et al. 2019) and [Te III] ($\lambda 21500$; e.g., Gillanders et al. 2023; Hotokezaka et al. 2023; Levan et al. 2023a). Further lines may be identified by future high-resolution optical-NIR spectroscopy of kilonovae, most notably by JWST. Future late-time spectroscopy during the nebular phase of GRB-SNe can then be used to measure or place deep limits on the ejecta mass produced of each element.

6. CONCLUSIONS

We have presented optical-NIR observations of four GRB-SNe extending out to $\delta t = 588$ days and search for signs of r -process enrichment in the context of the Barnes & Metzger (2022) models. Our dataset primarily consists of newly-analyzed observations from *HST*, with additional data from the VLT and the MMT. This analysis provides a template for considerations (e.g., afterglow, local extinction contamination) that may affect observational designs aimed at obtaining future color measurements of GRB-SNe. Moreover, combined with literature data, these observations can be used in comparison to future, enhanced models of r -process-enriched GRB-SNe, including those that account for viewing angle. Our analysis presents the first GRB-SNe sample of color measurements extending to the NIR at late times and allows us to make constraints on M_{rp} and ψ_{mix} for

individual objects. Based on our analysis we make the following conclusions:

- Comparing our observed colors to those from the models of Barnes & Metzger (2022), we find that GRB 190829A favors low or no r -process enrichment, while GRB 100316D may favor some enrichment at a moderate mixing fraction. For the other two GRBs, observations are not of sufficient signal-to-noise or on the correct timescales to adequately probe r -process enrichment, although overall we find GRB 030329 and 130427A are bluer than predicted by the model.
- Observations of GRB 100316D favor r -process enrichment of $M_{\text{rp}} = 0.03 - 0.15 M_{\odot}$ and $\psi_{\text{mix}} \lesssim 0.4$ while our dataset for GRB 190829A limits $M_{\text{rp}} \lesssim 0.01 M_{\odot}$ and $\psi_{\text{mix}} \leq 0.1$. We caution that our analysis is based on a fiducial set of semi-analytic models (Barnes & Metzger 2022) that is unable to account for $\gtrsim 30\%$ of our observations. Future modeling will improve on these conclusions.
- Taken together, our color observations of four events prefer lower values of ψ_{mix} . Our $R - H$ GRB-SNe color measurements are not significantly different compared to those of SN Ic-BL without GRBs (Anand et al. 2023), contrasting with predictions that the presence of a jet and a pole-on viewing angle results in larger observed ψ_{mix} (Barnes & Duffell 2023).
- GRBs 100316D and 190829A support theoretical predictions that GRBs with longer durations and lower SN initial explosion energies may produce higher values of ψ_{mix} (e.g., Barnes & Duffell 2023).
- We calculate the r -process enrichment from GRB-SNe and compare it to the observed Milky Way value from the literature. Considering our derived yields for GRBs 100315D and 190829A and the total Milky Way yield of Hotokezaka et al. (2018), GRB-SNe may produce 2 – 47% of the Milky Way’s r -process abundance. However, this fraction is highly uncertain, and will be improved with further understanding of r -process yields from GRB-SNe and rate estimates that consider low-luminosity GRBs.
- Building a statistically significant sample of inferences on ejecta mass from GRB-SNe requires large-aperture ground-based and space-based telescopes to monitor events at $\delta t \gtrsim 70$ days. The

cadence and long baseline of GRB 190829A observations is the archetype for future GRB-SN monitoring.

Despite the landmark discovery of r -process nucleosynthesis in a neutron star merger, it remains an open question as to whether other heavy element formation channels exist (e.g., Rosswog & Korobkin 2022). The rates of BNS mergers (e.g., The LIGO Scientific Collaboration et al. 2021; Mandel & Broekgaarden 2022; Rouco Escorial et al. 2022) as well as the mass and composition yields of kilonovae remain highly uncertain but likely vary widely (e.g., Gompertz et al. 2018; Metzger 2019; Kawaguchi et al. 2020; Rastinejad et al. 2021). The uncertainties in cosmological and Galactic BNS merger rates and their heavy element yields leave room for the existence of a second r -process formation channel (e.g., Holmbeck & Andrews 2023). At the same time, emerging observations of r -process-enriched metal-poor stellar populations indicate a source of heavy elements closely tracing star formation (e.g., Ji & Frebel 2018; Naidu et al. 2022; Ji et al. 2023; Simon et al. 2023; Kirby et al. 2023).

Moving forward, to identify or place deep constraints on r -process in rare classes of CCSNe requires significant effort and resources on both the theoretical and observational end. The development of observational predictions for r -process-enriched collapsar and MR SNe (or newly developed theories) is critical to establishing these sources as sites from photometric color measurements alone. Further late-time color and/or spectroscopic observations of GRB-SNe, SNe Ic-BL and, potentially, superluminous SNe (e.g., Reichert et al. 2023) will provide additional measurements or upper limits of their r -process yields. Though spectroscopic observations, especially with *JWST*, are critical to definitively establishing these events as sites of r -process element production, color measurements are possible for a greater volume of GRB-SNe, improving our understanding of the distribution of ejecta masses. Dedicated programs on space-based facilities such as *HST* and *JWST* are necessary for this late-time NIR follow-up. With unprecedented sensitivity in the NIR bands, the upcoming *Nancy Grace Roman* Space Telescope will be a critical facility for this field. Finally, these studies of some of the most promising candidates for r -process enrichment are not possible without the continued and ensured detection of well-localized GRBs by satellites such as *Swift* and its successors.

Facilities: *HST* (ACS, NICMOS, WFC3 and WFPC2), MMT (Binospec), VLT (HAWK-I, X-shooter)

Software: astropy (Astropy Collaboration et al. 2013, 2018), IRAF (Tody 1986, 1993), matplotlib, Numpy, SExtractor (Bertin & Arnouts 1996)

7. ACKNOWLEDGEMENTS

We gratefully acknowledge Jennifer Barnes, Steve Schulze, Huei Sears, Peter Blanchard and Alessandra Corsi for valuable conversations regarding this manuscript.

The Fong Group at Northwestern acknowledges support by the National Science Foundation under grant Nos. AST-1909358, AST-2206494, AST-2308182, and CAREER grant No. AST-2047919. W.F. gratefully acknowledges support by the David and Lucile Packard Foundation, the Alfred P. Sloan Foundation, and the Research Corporation for Science Advancement through Cottrell Scholar Award 28284. Support for this work was provided by the National Aeronautics and Space Administration through Chandra Award Number DD3-24139X issued by the Chandra X-ray Center, which is operated by the Smithsonian Astrophysical Observatory for and on behalf of the National Aeronautics Space Administration under contract NAS8-03060. G.P.L. is supported by a Royal Society Dorothy Hodgkin Fellowship (grant Nos. DHF-R1-221175 and DHF-ERE-221005). G.S. and P.S. acknowledge the support by the State of Hesse within the Research Cluster ELEMENTS (Project ID 500/10.006). E.P. acknowledges financial support through INAF Fundamental Research Grant 2022. L.I. was supported by an INAF Fundamental Research Grant 2023. S. Anand acknowledges support from the National Science Foundation GROWTH PIRE grant No. 1545949.

Based on observations made with the NASA/ESA Hubble Space Telescope, obtained from the data archive at the Space Telescope Science Institute. STScI is operated by the Association of Universities for Research in Astronomy, Inc. under NASA contract NAS 5-26555. Observations reported here were obtained at the MMT Observatory, a joint facility of the University of Arizona and the Smithsonian Institution. MMT Observatory access was supported by Northwestern University and the Center for Interdisciplinary Exploration and Research in Astrophysics (CIERA). Based on observations collected at the European Organisation for Astronomical Research in the Southern Hemisphere. This research has made use of NASA’s Astrophysics Data System.

REFERENCES

- Abbott, B. P., Abbott, R., Abbott, T. D., et al. 2017a, *ApJL*, 848, L12, doi: [10.3847/2041-8213/aa91c9](https://doi.org/10.3847/2041-8213/aa91c9)
- . 2017b, *ApJL*, 848, L13, doi: [10.3847/2041-8213/aa920c](https://doi.org/10.3847/2041-8213/aa920c)
- Ackermann, M., Ajello, M., Asano, K., et al. 2014, *Science*, 343, 42, doi: [10.1126/science.1242353](https://doi.org/10.1126/science.1242353)
- Alam, S., Albareti, F. D., Allende Prieto, C., et al. 2015, *ApJS*, 219, 12, doi: [10.1088/0067-0049/219/1/12](https://doi.org/10.1088/0067-0049/219/1/12)
- Anand, S., Barnes, J., Yang, S., et al. 2023, arXiv e-prints, arXiv:2302.09226, doi: [10.48550/arXiv.2302.09226](https://doi.org/10.48550/arXiv.2302.09226)
- Arcavi, I., Hosseinzadeh, G., Howell, D. A., et al. 2017, *Nature*, 551, 64, doi: [10.1038/nature24291](https://doi.org/10.1038/nature24291)
- Arcones, A., Janka, H. T., & Scheck, L. 2007, *A&A*, 467, 1227, doi: [10.1051/0004-6361/20066983](https://doi.org/10.1051/0004-6361/20066983)
- Arnett, W. D. 1982, *ApJ*, 253, 785, doi: [10.1086/159681](https://doi.org/10.1086/159681)
- Astropy Collaboration, Robitaille, T. P., Tollerud, E. J., et al. 2013, *A&A*, 558, A33, doi: [10.1051/0004-6361/201322068](https://doi.org/10.1051/0004-6361/201322068)
- Astropy Collaboration, Price-Whelan, A. M., Sipőcz, B. M., et al. 2018, *AJ*, 156, 123, doi: [10.3847/1538-3881/aabc4f](https://doi.org/10.3847/1538-3881/aabc4f)
- Barnes, J., & Duffell, P. C. 2023, arXiv e-prints, arXiv:2305.00056, doi: [10.48550/arXiv.2305.00056](https://doi.org/10.48550/arXiv.2305.00056)
- Barnes, J., & Metzger, B. D. 2022, *ApJL*, 939, L29, doi: [10.3847/2041-8213/ac9b41](https://doi.org/10.3847/2041-8213/ac9b41)
- Battistini, C., & Bensby, T. 2016, *A&A*, 586, A49, doi: [10.1051/0004-6361/201527385](https://doi.org/10.1051/0004-6361/201527385)
- Bauswein, A., Ardevol Pulpillo, R., Janka, H. T., & Goriely, S. 2014, *ApJL*, 795, L9, doi: [10.1088/2041-8205/795/1/L9](https://doi.org/10.1088/2041-8205/795/1/L9)
- Becker, A. 2015, HOTPANTS: High Order Transform of PSF ANd Template Subtraction. <http://ascl.net/1504.004>
- Belczynski, K., Kalogera, V., & Bulik, T. 2002, *ApJ*, 572, 407, doi: [10.1086/340304](https://doi.org/10.1086/340304)
- Bennett, C. L., Larson, D., Weiland, J. L., & Hinshaw, G. 2014, *ApJ*, 794, 135, doi: [10.1088/0004-637X/794/2/135](https://doi.org/10.1088/0004-637X/794/2/135)
- Bertin, E., & Arnouts, S. 1996, *A&AS*, 117, 393, doi: [10.1051/aas:1996164](https://doi.org/10.1051/aas:1996164)
- Blanchard, P. K., Berger, E., & Fong, W.-f. 2016, *ApJ*, 817, 144, doi: [10.3847/0004-637X/817/2/144](https://doi.org/10.3847/0004-637X/817/2/144)
- Blanchard, P. K., Villar, V. A., Chornock, R., et al. 2023, arXiv e-prints, arXiv:2308.14197, doi: [10.48550/arXiv.2308.14197](https://doi.org/10.48550/arXiv.2308.14197)
- Bohlin, R. C. 2016, *AJ*, 152, 60, doi: [10.3847/0004-6256/152/3/60](https://doi.org/10.3847/0004-6256/152/3/60)
- Bufano, F., Pian, E., Sollerman, J., et al. 2012, *ApJ*, 753, 67, doi: [10.1088/0004-637X/753/1/67](https://doi.org/10.1088/0004-637X/753/1/67)
- Burbidge, E. M., Burbidge, G. R., Fowler, W. A., & Hoyle, F. 1957, *Reviews of Modern Physics*, 29, 547, doi: [10.1103/RevModPhys.29.547](https://doi.org/10.1103/RevModPhys.29.547)
- Burns, E., Svinkin, D., Fenimore, E., et al. 2023, *ApJL*, 946, L31, doi: [10.3847/2041-8213/acc39c](https://doi.org/10.3847/2041-8213/acc39c)
- Cameron, A. G. W. 1957, *AJ*, 62, 9, doi: [10.1086/107435](https://doi.org/10.1086/107435)
- . 2003, *ApJ*, 587, 327, doi: [10.1086/368110](https://doi.org/10.1086/368110)
- Cano, Z., Wang, S.-Q., Dai, Z.-G., & Wu, X.-F. 2017a, *Advances in Astronomy*, 2017, 8929054, doi: [10.1155/2017/8929054](https://doi.org/10.1155/2017/8929054)
- Cano, Z., Bersier, D., Guidorzi, C., et al. 2011, *ApJ*, 740, 41, doi: [10.1088/0004-637X/740/1/41](https://doi.org/10.1088/0004-637X/740/1/41)
- Cano, Z., Izzo, L., de Ugarte Postigo, A., et al. 2017b, *A&A*, 605, A107, doi: [10.1051/0004-6361/201731005](https://doi.org/10.1051/0004-6361/201731005)
- Cardelli, J. A., Clayton, G. C., & Mathis, J. S. 1989, *ApJ*, 345, 245, doi: [10.1086/167900](https://doi.org/10.1086/167900)
- Chand, V., Banerjee, A., Gupta, R., et al. 2020, *ApJ*, 898, 42, doi: [10.3847/1538-4357/ab9606](https://doi.org/10.3847/1538-4357/ab9606)
- Chornock, R., Berger, E., Levesque, E. M., et al. 2010, arXiv e-prints, arXiv:1004.2262, doi: [10.48550/arXiv.1004.2262](https://doi.org/10.48550/arXiv.1004.2262)
- Côté, B., Belczynski, K., Fryer, C. L., & et al. 2017, *ApJ*, 836, 230, doi: [10.3847/1538-4357/aa5c8d](https://doi.org/10.3847/1538-4357/aa5c8d)
- Coulter, D. A., Foley, R. J., Kilpatrick, C. D., et al. 2017, *Science*, 358, 1556, doi: [10.1126/science.aap9811](https://doi.org/10.1126/science.aap9811)
- Cowan, J. J., Sneden, C., Lawler, J. E., et al. 2021, *Reviews of Modern Physics*, 93, 015002, doi: [10.1103/RevModPhys.93.015002](https://doi.org/10.1103/RevModPhys.93.015002)
- Cowan, J. J., Thielemann, F.-K., & Truran, J. W. 1991, *PhR*, 208, 267, doi: [10.1016/0370-1573\(91\)90070-3](https://doi.org/10.1016/0370-1573(91)90070-3)
- Dainotti, M. G., De Simone, B., Islam, K. M., et al. 2022, *ApJ*, 938, 41, doi: [10.3847/1538-4357/ac8b77](https://doi.org/10.3847/1538-4357/ac8b77)
- De, S., & Siegel, D. M. 2021, *ApJ*, 921, 94, doi: [10.3847/1538-4357/ac110b](https://doi.org/10.3847/1538-4357/ac110b)
- De Pasquale, M., Page, M. J., Kann, D. A., et al. 2016, *MNRAS*, 462, 1111, doi: [10.1093/mnras/stw1704](https://doi.org/10.1093/mnras/stw1704)
- Dichiara, S., Bernardini, M. G., Burrows, D. N., et al. 2019, *GRB Coordinates Network*, 25552, 1
- Dichiara, S., Troja, E., Lipunov, V., et al. 2022, *MNRAS*, 512, 2337, doi: [10.1093/mnras/stac454](https://doi.org/10.1093/mnras/stac454)
- Dominik, M., Belczynski, K., Fryer, C., et al. 2012, *ApJ*, 759, 52, doi: [10.1088/0004-637X/759/1/52](https://doi.org/10.1088/0004-637X/759/1/52)
- Evans, P. A., Willingale, R., Osborne, J. P., et al. 2014, *MNRAS*, 444, 250, doi: [10.1093/mnras/stu1459](https://doi.org/10.1093/mnras/stu1459)
- Fermi GBM Team. 2019, *GRB Coordinates Network*, 25551, 1
- Fischer, T., Whitehouse, S. C., Mezzacappa, A., Thielemann, F. K., & Liebendörfer, M. 2010, *A&A*, 517, A80, doi: [10.1051/0004-6361/200913106](https://doi.org/10.1051/0004-6361/200913106)
- Fong, W.-f., Nugent, A. E., Dong, Y., et al. 2022, *ApJ*, 940, 56, doi: [10.3847/1538-4357/ac91d0](https://doi.org/10.3847/1538-4357/ac91d0)

- Frebel, A. 2018, *Annual Review of Nuclear and Particle Science*, 68, 237, doi: [10.1146/annurev-nucl-101917-021141](https://doi.org/10.1146/annurev-nucl-101917-021141)
- Fruchter, A. S., Levan, A. J., Strolger, L., et al. 2006, *Nature*, 441, 463, doi: [10.1038/nature04787](https://doi.org/10.1038/nature04787)
- Fujibayashi, S., Sekiguchi, Y., Shibata, M., & Wanaajo, S. 2022, arXiv e-prints, arXiv:2212.03958, doi: [10.48550/arXiv.2212.03958](https://doi.org/10.48550/arXiv.2212.03958)
- Gehrels, N., Chincarini, G., Giommi, P., et al. 2004, *ApJ*, 611, 1005, doi: [10.1086/422091](https://doi.org/10.1086/422091)
- Ghirlanda, G., Nava, L., Ghisellini, G., & Firmani, C. 2007, *A&A*, 466, 127, doi: [10.1051/0004-6361:20077119](https://doi.org/10.1051/0004-6361:20077119)
- Ghirlanda, G., & Salvaterra, R. 2022, *ApJ*, 932, 10, doi: [10.3847/1538-4357/ac6e43](https://doi.org/10.3847/1538-4357/ac6e43)
- Gillanders, J. H., Troja, E., Fryer, C. L., et al. 2023, arXiv e-prints, arXiv:2308.00633, doi: [10.48550/arXiv.2308.00633](https://doi.org/10.48550/arXiv.2308.00633)
- Goldstein, A., Veres, P., Burns, E., et al. 2017, *The Astrophysical Journal*, 848, L14, doi: [10.3847/2041-8213/aa8f41](https://doi.org/10.3847/2041-8213/aa8f41)
- Gompertz, B. P., Levan, A. J., Tanvir, N. R., et al. 2018, *ApJ*, 860, 62, doi: [10.3847/1538-4357/aac206](https://doi.org/10.3847/1538-4357/aac206)
- Gonzaga, S., Hack, W., Fruchter, A., & Mack, J. 2012, *The DrizzlePac Handbook*
- Gordon, K. D., Clayton, G. C., Misselt, K. A., Landolt, A. U., & Wolff, M. J. 2003, *ApJ*, 594, 279, doi: [10.1086/376774](https://doi.org/10.1086/376774)
- Greiner, J., Peimbert, M., Esteban, C., et al. 2003, *GRB Coordinates Network*, 2020, 1
- Greiner, J., Mazzali, P. A., Kann, D. A., et al. 2015, *Nature*, 523, 189, doi: [10.1038/nature14579](https://doi.org/10.1038/nature14579)
- H. E. S. S. Collaboration, Abdalla, H., Aharonian, F., et al. 2021, *Science*, 372, 1081, doi: [10.1126/science.abe8560](https://doi.org/10.1126/science.abe8560)
- Halevi, G., & Mösta, P. 2018, *MNRAS*, 477, 2366, doi: [10.1093/mnras/sty797](https://doi.org/10.1093/mnras/sty797)
- Hansen, T. T., Simon, J. D., Marshall, J. L., et al. 2017, *ApJ*, 838, 44, doi: [10.3847/1538-4357/aa634a](https://doi.org/10.3847/1538-4357/aa634a)
- Hjorth, J., Sollerman, J., Møller, P., et al. 2003, *Nature*, 423, 847, doi: [10.1038/nature01750](https://doi.org/10.1038/nature01750)
- Hoffman, R. D., Woosley, S. E., & Qian, Y. Z. 1997, *ApJ*, 482, 951, doi: [10.1086/304181](https://doi.org/10.1086/304181)
- Holmbeck, E. M., & Andrews, J. J. 2023, arXiv e-prints, arXiv:2310.03847, doi: [10.48550/arXiv.2310.03847](https://doi.org/10.48550/arXiv.2310.03847)
- Hosseinzadeh, G., Sand, D. J., Jencson, J. E., et al. 2023, *ApJL*, 942, L18, doi: [10.3847/2041-8213/aca64e](https://doi.org/10.3847/2041-8213/aca64e)
- Hotokezaka, K., Beniamini, P., & Piran, T. 2018, *International Journal of Modern Physics D*, 27, 1842005, doi: [10.1142/S0218271818420051](https://doi.org/10.1142/S0218271818420051)
- Hotokezaka, K., Tanaka, M., Kato, D., & Gaigalas, G. 2023, arXiv e-prints, arXiv:2307.00988, doi: [10.48550/arXiv.2307.00988](https://doi.org/10.48550/arXiv.2307.00988)
- Hu, Y. D., Castro-Tirado, A. J., Kumar, A., et al. 2021, *A&A*, 646, A50, doi: [10.1051/0004-6361/202039349](https://doi.org/10.1051/0004-6361/202039349)
- Huang, J.-K., Huang, X.-L., Cheng, J.-G., et al. 2023, *ApJ*, 947, 84, doi: [10.3847/1538-4357/acc85f](https://doi.org/10.3847/1538-4357/acc85f)
- Ji, A. P., & Frebel, A. 2018, *ApJ*, 856, 138, doi: [10.3847/1538-4357/aab14a](https://doi.org/10.3847/1538-4357/aab14a)
- Ji, A. P., Frebel, A., Chiti, A., & Simon, J. D. 2016, *Nature*, 531, 610, doi: [10.1038/nature17425](https://doi.org/10.1038/nature17425)
- Ji, A. P., Simon, J. D., Roederer, I. U., et al. 2023, *AJ*, 165, 100, doi: [10.3847/1538-3881/acad84](https://doi.org/10.3847/1538-3881/acad84)
- Just, O., Aloy, M. A., Obergaulinger, M., & Nagataki, S. 2022, *ApJL*, 934, L30, doi: [10.3847/2041-8213/ac83a1](https://doi.org/10.3847/2041-8213/ac83a1)
- Kamble, A., Horst, A. J. V., Bhattacharya, D., et al. 2009, in *Astronomical Society of the Pacific Conference Series*, Vol. 407, *The Low-Frequency Radio Universe*, ed. D. J. Saikia, D. A. Green, Y. Gupta, & T. Venturi, 295
- Kann, D. A., Klose, S., & Zeh, A. 2006, *ApJ*, 641, 993, doi: [10.1086/500652](https://doi.org/10.1086/500652)
- Kasen, D., Metzger, B., Barnes, J., Quataert, E., & Ramirez-Ruiz, E. 2017, *Nature*, 551, 80, doi: [10.1038/nature24453](https://doi.org/10.1038/nature24453)
- Kawabata, K. S., Deng, J., Wang, L., et al. 2003, *ApJL*, 593, L19, doi: [10.1086/378148](https://doi.org/10.1086/378148)
- Kawaguchi, K., Shibata, M., & Tanaka, M. 2020, *ApJ*, 889, 171, doi: [10.3847/1538-4357/ab61f6](https://doi.org/10.3847/1538-4357/ab61f6)
- Kilpatrick, C. D., Izzo, L., Bentley, R. O., et al. 2023, *MNRAS*, 524, 2161, doi: [10.1093/mnras/stad1954](https://doi.org/10.1093/mnras/stad1954)
- Kirby, E. N., Duggan, G., Ramirez-Ruiz, E., & et al. 2020, *ApJL*, 891, L13, doi: [10.3847/2041-8213/ab78a1](https://doi.org/10.3847/2041-8213/ab78a1)
- Kirby, E. N., Ji, A. P., & Kovalev, M. 2023, *ApJ*, 958, 45, doi: [10.3847/1538-4357/acf309](https://doi.org/10.3847/1538-4357/acf309)
- Laskar, T., Berger, E., Zauderer, B. A., et al. 2013, *ApJ*, 776, 119, doi: [10.1088/0004-637X/776/2/119](https://doi.org/10.1088/0004-637X/776/2/119)
- Lattimer, J. M., & Schramm, D. N. 1974, *ApJL*, 192, L145, doi: [10.1086/181612](https://doi.org/10.1086/181612)
- Lee, K. H., Bartos, I., Eddins, A., et al. 2022, *ApJL*, 934, L5, doi: [10.3847/2041-8213/ac7ff0](https://doi.org/10.3847/2041-8213/ac7ff0)
- Levan, A., Gompertz, B. P., Salafia, O. S., et al. 2023a, arXiv e-prints, arXiv:2307.02098, doi: [10.48550/arXiv.2307.02098](https://doi.org/10.48550/arXiv.2307.02098)
- Levan, A. J., Cenko, S. B., Perley, D. A., & Tanvir, N. R. 2013, *GRB Coordinates Network*, 14455, 1
- Levan, A. J., Tanvir, N. R., Fruchter, A. S., et al. 2014a, *ApJ*, 792, 115, doi: [10.1088/0004-637X/792/2/115](https://doi.org/10.1088/0004-637X/792/2/115)
- Levan, A. J., Tanvir, N. R., Starling, R. L. C., et al. 2014b, *ApJ*, 781, 13, doi: [10.1088/0004-637X/781/1/13](https://doi.org/10.1088/0004-637X/781/1/13)

- Levan, A. J., Lamb, G. P., Schneider, B., et al. 2023b, *ApJL*, 946, L28, doi: [10.3847/2041-8213/acc2c1](https://doi.org/10.3847/2041-8213/acc2c1)
- Li, L., Zhong, S.-Q., & Dai, Z.-G. 2023, arXiv e-prints, arXiv:2307.09917. <https://arxiv.org/abs/2307.09917>
- Lipkin, Y. M., Ofek, E. O., Gal-Yam, A., et al. 2004, *ApJ*, 606, 381, doi: [10.1086/383000](https://doi.org/10.1086/383000)
- Lipunov, V. M., Gorbovskoy, E., Kornilov, V. G., et al. 2017, *ApJL*, 850, L1, doi: [10.3847/2041-8213/aa92c0](https://doi.org/10.3847/2041-8213/aa92c0)
- Lyman, J. D., Levan, A. J., Tanvir, N. R., et al. 2017, *MNRAS*, 467, 1795, doi: [10.1093/mnras/stx220](https://doi.org/10.1093/mnras/stx220)
- MacFadyen, A. I., & Woosley, S. E. 1999, *ApJ*, 524, 262, doi: [10.1086/307790](https://doi.org/10.1086/307790)
- Macias, P., & Ramirez-Ruiz, E. 2018, *ApJ*, 860, 89, doi: [10.3847/1538-4357/aac3e0](https://doi.org/10.3847/1538-4357/aac3e0)
- Mandel, I., & Broekgaarden, F. S. 2022, *Living Reviews in Relativity*, 25, 1, doi: [10.1007/s41114-021-00034-3](https://doi.org/10.1007/s41114-021-00034-3)
- Mandhai, S., Lamb, G. P., Tanvir, N. R., et al. 2022, *MNRAS*, 514, 2716, doi: [10.1093/mnras/stac1473](https://doi.org/10.1093/mnras/stac1473)
- Margutti, R., Soderberg, A. M., Wieringa, M. H., et al. 2013, *ApJ*, 778, 18, doi: [10.1088/0004-637X/778/1/18](https://doi.org/10.1088/0004-637X/778/1/18)
- Martínez-Pinedo, G., Fischer, T., Lohs, A., & Huther, L. 2012, *PhRvL*, 109, 251104, doi: [10.1103/PhysRevLett.109.251104](https://doi.org/10.1103/PhysRevLett.109.251104)
- Martínez-Pinedo, G., Lam, Y. H., Langanke, K., Zegers, R. G. T., & Sullivan, C. 2014, *PhRvC*, 89, 045806, doi: [10.1103/PhysRevC.89.045806](https://doi.org/10.1103/PhysRevC.89.045806)
- Maselli, A., Melandri, A., Nava, L., et al. 2014, *Science*, 343, 48, doi: [10.1126/science.1242279](https://doi.org/10.1126/science.1242279)
- Matheson, T., Garnavich, P. M., Stanek, K. Z., et al. 2003, *ApJ*, 599, 394, doi: [10.1086/379228](https://doi.org/10.1086/379228)
- Mazzali, P. A., Pian, E., Bufano, F., & Ashall, C. 2021, *MNRAS*, 505, 4106, doi: [10.1093/mnras/stab1594](https://doi.org/10.1093/mnras/stab1594)
- Mazzali, P. A., Deng, J., Tominaga, N., et al. 2003, *ApJL*, 599, L95, doi: [10.1086/381259](https://doi.org/10.1086/381259)
- Meegan, C., Lichti, G., Bhat, P. N., et al. 2009, *ApJ*, 702, 791, doi: [10.1088/0004-637X/702/1/791](https://doi.org/10.1088/0004-637X/702/1/791)
- Melandri, A., Pian, E., D'Elia, V., et al. 2014, *A&A*, 567, A29, doi: [10.1051/0004-6361/201423572](https://doi.org/10.1051/0004-6361/201423572)
- Metzger, B. D. 2019, *Living Reviews in Relativity*, 23, 1, doi: [10.1007/s41114-019-0024-0](https://doi.org/10.1007/s41114-019-0024-0)
- Metzger, B. D., Piro, A. L., & Quataert, E. 2009, *MNRAS*, 396, 304, doi: [10.1111/j.1365-2966.2008.14380.x](https://doi.org/10.1111/j.1365-2966.2008.14380.x)
- Metzger, B. D., Thompson, T. A., & Quataert, E. 2007, *ApJ*, 659, 561, doi: [10.1086/512059](https://doi.org/10.1086/512059)
- Miller, J. M., Sprouse, T. M., Fryer, C. L., et al. 2020, *ApJ*, 902, 66, doi: [10.3847/1538-4357/abb4e3](https://doi.org/10.3847/1538-4357/abb4e3)
- Modjaz, M., Liu, Y. Q., Bianco, F. B., & Graur, O. 2016, *ApJ*, 832, 108, doi: [10.3847/0004-637X/832/2/108](https://doi.org/10.3847/0004-637X/832/2/108)
- Moss, M. J., Mochkovitch, R., Daigne, F., Beniamini, P., & Guiriec, S. 2023, arXiv e-prints, arXiv:2306.00815, doi: [10.48550/arXiv.2306.00815](https://doi.org/10.48550/arXiv.2306.00815)
- Mösta, P., Ott, C. D., Radice, D., et al. 2015, *Nature*, 528, 376, doi: [10.1038/nature15755](https://doi.org/10.1038/nature15755)
- Mösta, P., Roberts, L. F., Halevi, G., et al. 2018, *ApJ*, 864, 171, doi: [10.3847/1538-4357/aad6ec](https://doi.org/10.3847/1538-4357/aad6ec)
- Naidu, R. P., Ji, A. P., Conroy, C., et al. 2022, *ApJL*, 926, L36, doi: [10.3847/2041-8213/ac5589](https://doi.org/10.3847/2041-8213/ac5589)
- Nugent, A. E., Fong, W.-f., Castrejon, C., et al. 2023, arXiv e-prints, arXiv:2310.12202. <https://arxiv.org/abs/2310.12202>
- Nugent, A. E., Fong, W.-F., Dong, Y., et al. 2022, *ApJ*, 940, 57, doi: [10.3847/1538-4357/ac91d1](https://doi.org/10.3847/1538-4357/ac91d1)
- O'Connor, B., Troja, E., Dichiaro, S., et al. 2022, *MNRAS*, 515, 4890, doi: [10.1093/mnras/stac1982](https://doi.org/10.1093/mnras/stac1982)
- Olivares E., F., Greiner, J., Schady, P., et al. 2012, *A&A*, 539, A76, doi: [10.1051/0004-6361/201117929](https://doi.org/10.1051/0004-6361/201117929)
- Östlin, G., Zackrisson, E., Sollerman, J., Mattila, S., & Hayes, M. 2008, *MNRAS*, 387, 1227, doi: [10.1111/j.1365-2966.2008.13319.x](https://doi.org/10.1111/j.1365-2966.2008.13319.x)
- Perley, D. A., Cenko, S. B., Corsi, A., et al. 2014, *ApJ*, 781, 37, doi: [10.1088/0004-637X/781/1/37](https://doi.org/10.1088/0004-637X/781/1/37)
- Perley, D. A., Fremling, C., Sollerman, J., et al. 2020, *ApJ*, 904, 35, doi: [10.3847/1538-4357/abbd98](https://doi.org/10.3847/1538-4357/abbd98)
- Piro, L., Troja, E., Gendre, B., et al. 2014, *ApJL*, 790, L15, doi: [10.1088/2041-8205/790/2/L15](https://doi.org/10.1088/2041-8205/790/2/L15)
- Prentice, S. J., Ashall, C., James, P. A., et al. 2019, *MNRAS*, 485, 1559, doi: [10.1093/mnras/sty3399](https://doi.org/10.1093/mnras/sty3399)
- Rastinejad, J. C., Fong, W., Kilpatrick, C. D., et al. 2021, *ApJ*, 916, 89, doi: [10.3847/1538-4357/ac04b4](https://doi.org/10.3847/1538-4357/ac04b4)
- Rastinejad, J. C., Gompertz, B. P., Levan, A. J., et al. 2022, *Nature*, 612, 223, doi: [10.1038/s41586-022-05390-w](https://doi.org/10.1038/s41586-022-05390-w)
- Reichert, M., Obergaulinger, M., Aloy, M. Á., et al. 2023, *MNRAS*, 518, 1557, doi: [10.1093/mnras/stac3185](https://doi.org/10.1093/mnras/stac3185)
- Rhodes, L., van der Horst, A. J., Fender, R., et al. 2020, *MNRAS*, 496, 3326, doi: [10.1093/mnras/staa1715](https://doi.org/10.1093/mnras/staa1715)
- Rosswog, S., & Korobkin, O. 2022, arXiv e-prints, arXiv:2208.14026, doi: [10.48550/arXiv.2208.14026](https://doi.org/10.48550/arXiv.2208.14026)
- Rosswog, S., Liebendörfer, M., Thielemann, F. K., et al. 1999, *A&A*, 341, 499, doi: [10.48550/arXiv.astro-ph/9811367](https://doi.org/10.48550/arXiv.astro-ph/9811367)
- Rosswog, S., Sollerman, J., Feindt, U., et al. 2018, *A&A*, 615, A132, doi: [10.1051/0004-6361/201732117](https://doi.org/10.1051/0004-6361/201732117)
- Rouco Escorial, A., Fong, W.-f., Berger, E., et al. 2022, arXiv e-prints, arXiv:2210.05695, doi: [10.48550/arXiv.2210.05695](https://doi.org/10.48550/arXiv.2210.05695)
- Sakamoto, T., Barthelmy, S. D., Baumgartner, W. H., et al. 2010, *GRB Coordinates Network*, 10511, 1

- Savchenko, V., Ferrigno, C., Kuulkers, E., et al. 2017, *ApJL*, 848, L15, doi: [10.3847/2041-8213/aa8f94](https://doi.org/10.3847/2041-8213/aa8f94)
- Schady, P., Dwelly, T., Page, M. J., et al. 2012, *A&A*, 537, A15, doi: [10.1051/0004-6361/201117414](https://doi.org/10.1051/0004-6361/201117414)
- Schlaflly, E. F., & Finkbeiner, D. P. 2011, *ApJ*, 737, 103, doi: [10.1088/0004-637X/737/2/103](https://doi.org/10.1088/0004-637X/737/2/103)
- Shahbandeh, M., Sarangi, A., Temim, T., et al. 2023, *MNRAS*, 523, 6048, doi: [10.1093/mnras/stad1681](https://doi.org/10.1093/mnras/stad1681)
- Shen, S., Cooke, R. J., Ramirez-Ruiz, E., et al. 2015, *ApJ*, 807, 115, doi: [10.1088/0004-637X/807/2/115](https://doi.org/10.1088/0004-637X/807/2/115)
- Siegel, D. M., Barnes, J., & Metzger, B. D. 2019, *Nature*, 569, 241, doi: [10.1038/s41586-019-1136-0](https://doi.org/10.1038/s41586-019-1136-0)
- Simon, J. D., Brown, T. M., Mutlu-Pakdil, B., et al. 2023, *ApJ*, 944, 43, doi: [10.3847/1538-4357/aca9d1](https://doi.org/10.3847/1538-4357/aca9d1)
- Skrutskie, M. F., Cutri, R. M., Stiening, R., et al. 2006, *AJ*, 131, 1163, doi: [10.1086/498708](https://doi.org/10.1086/498708)
- Soares-Santos, M., Holz, D. E., Annis, J., et al. 2017, *ApJL*, 848, L16, doi: [10.3847/2041-8213/aa9059](https://doi.org/10.3847/2041-8213/aa9059)
- Stanek, K. Z., Matheson, T., Garnavich, P. M., et al. 2003, *ApJL*, 591, L17, doi: [10.1086/376976](https://doi.org/10.1086/376976)
- Starling, R. L. C., Wiersema, K., Levan, A. J., et al. 2011, *MNRAS*, 411, 2792, doi: [10.1111/j.1365-2966.2010.17879.x](https://doi.org/10.1111/j.1365-2966.2010.17879.x)
- Szalai, T., Fox, O. D., Arendt, R. G., et al. 2021, *ApJ*, 919, 17, doi: [10.3847/1538-4357/ac0e2b](https://doi.org/10.3847/1538-4357/ac0e2b)
- Tanvir, N. R., Levan, A. J., González-Fernández, C., et al. 2017, *ApJL*, 848, L27, doi: [10.3847/2041-8213/aa90b6](https://doi.org/10.3847/2041-8213/aa90b6)
- Tauris, T. M., Kramer, M., Freire, P. C. C., et al. 2017, *ApJ*, 846, 170, doi: [10.3847/1538-4357/aa7e89](https://doi.org/10.3847/1538-4357/aa7e89)
- The LIGO Scientific Collaboration, the Virgo Collaboration, the KAGRA Collaboration, et al. 2021, arXiv e-prints, arXiv:2111.03606. <https://arxiv.org/abs/2111.03606>
- Thielemann, F. K., Arcones, A., Käppeli, R., et al. 2011, *Progress in Particle and Nuclear Physics*, 66, 346, doi: [10.1016/j.pnpnp.2011.01.032](https://doi.org/10.1016/j.pnpnp.2011.01.032)
- Thompson, T. A., Chang, P., & Quataert, E. 2004, *ApJ*, 611, 380, doi: [10.1086/421969](https://doi.org/10.1086/421969)
- Thompson, T. A., & ud-Doula, A. 2018, *MNRAS*, 476, 5502, doi: [10.1093/mnras/sty480](https://doi.org/10.1093/mnras/sty480)
- Tiengo, A., Mereghetti, S., Ghisellini, G., Tavecchio, F., & Ghirlanda, G. 2004, *A&A*, 423, 861, doi: [10.1051/0004-6361:20041027](https://doi.org/10.1051/0004-6361:20041027)
- Tinyanont, S., Ridden-Harper, R., Foley, R. J., et al. 2022, *MNRAS*, 512, 2777, doi: [10.1093/mnras/stab2887](https://doi.org/10.1093/mnras/stab2887)
- Tody, D. 1986, in Society of Photo-Optical Instrumentation Engineers (SPIE) Conference Series, Vol. 627, Instrumentation in astronomy VI, ed. D. L. Crawford, 733, doi: [10.1117/12.968154](https://doi.org/10.1117/12.968154)
- Tody, D. 1993, in Astronomical Society of the Pacific Conference Series, Vol. 52, Astronomical Data Analysis Software and Systems II, ed. R. J. Hanisch, R. J. V. Brissenden, & J. Barnes, 173
- Troja, E., Fryer, C. L., O'Connor, B., et al. 2022, *Nature*, 612, 228, doi: [10.1038/s41586-022-05327-3](https://doi.org/10.1038/s41586-022-05327-3)
- Tsujimoto, T., & Shigeyama, T. 2001, *ApJL*, 561, L97, doi: [10.1086/324441](https://doi.org/10.1086/324441)
- Tsvetkova, A., Golenetskii, S., Aptekar, R., et al. 2019, GRB Coordinates Network, 25660, 1
- Valenti, S., Sand, D. J., Yang, S., et al. 2017, *ApJL*, 848, L24, doi: [10.3847/2041-8213/aa8edf](https://doi.org/10.3847/2041-8213/aa8edf)
- van de Voort, F., Pakmor, R., Bieri, R., & Grand, R. J. J. 2022, *MNRAS*, 512, 5258, doi: [10.1093/mnras/stac710](https://doi.org/10.1093/mnras/stac710)
- Vanderspek, R., Crew, G., Doty, J., et al. 2003, GRB Coordinates Network, 1997, 1
- Venn, K. A., Irwin, M., Shetrone, M. D., et al. 2004, *AJ*, 128, 1177, doi: [10.1086/422734](https://doi.org/10.1086/422734)
- von Kienlin, A. 2013, GRB Coordinates Network, 14473, 1
- Wallner, A., Faestermann, T., Feige, J., et al. 2015, *Nature Communications*, 6, 5956, doi: [10.1038/ncomms6956](https://doi.org/10.1038/ncomms6956)
- Wallner, A., Froehlich, M. B., Hotchkis, M. A. C., et al. 2021, *Science*, 372, 742, doi: [10.1126/science.aax3972](https://doi.org/10.1126/science.aax3972)
- Wang, T., & Burrows, A. 2023, arXiv e-prints, arXiv:2311.03446. <https://arxiv.org/abs/2311.03446>
- Watson, D., Hansen, C. J., Selsing, J., et al. 2019, *Nature*, 574, 497, doi: [10.1038/s41586-019-1676-3](https://doi.org/10.1038/s41586-019-1676-3)
- Williams, M. A., Kennea, J. A., Dichiara, S., et al. 2023, *ApJL*, 946, L24, doi: [10.3847/2041-8213/acbcd1](https://doi.org/10.3847/2041-8213/acbcd1)
- Woosley, S. E., Wilson, J. R., Mathews, G. J., Hoffman, R. D., & Meyer, B. S. 1994, *ApJ*, 433, 229, doi: [10.1086/174638](https://doi.org/10.1086/174638)
- Xu, D., de Ugarte Postigo, A., Leloudas, G., et al. 2013, *ApJ*, 776, 98, doi: [10.1088/0004-637X/776/2/98](https://doi.org/10.1088/0004-637X/776/2/98)
- Yang, J., Ai, S., Zhang, B.-B., et al. 2022, *Nature*, 612, 232, doi: [10.1038/s41586-022-05403-8](https://doi.org/10.1038/s41586-022-05403-8)
- Yang, Y.-H., Troja, E., O'Connor, B., et al. 2023, arXiv e-prints, arXiv:2308.00638, doi: [10.48550/arXiv.2308.00638](https://doi.org/10.48550/arXiv.2308.00638)
- Zenati, Y., Siegel, D. M., Metzger, B. D., & Perets, H. B. 2020, *MNRAS*, 499, 4097, doi: [10.1093/mnras/staa3002](https://doi.org/10.1093/mnras/staa3002)
- Zevin, M., Kremer, K., Siegel, D. M., et al. 2019, *ApJ*, 886, 4, doi: [10.3847/1538-4357/ab498b](https://doi.org/10.3847/1538-4357/ab498b)
- Zevin, M., Nugent, A. E., Adhikari, S., et al. 2022, *ApJL*, 940, L18, doi: [10.3847/2041-8213/ac91cd](https://doi.org/10.3847/2041-8213/ac91cd)

8. SUPPLEMENTARY INFORMATION

Table 2. Sample of Observations

GRB	z	Tel./Instum.	δt_{rest} (days)	Filter	Magnitude [†] (AB mag)	Error (AB mag)	Reference
030329	0.1685	Clay	0.6	<i>R</i>	15.23*	0.02	Matheson et al. (2003)
		Clay	0.6	<i>R</i>	15.2*	0.02	
		FLWO	0.6	<i>R</i>	15.39*	0.01	
		FLWO	0.6	<i>R</i>	15.38*	0.01	
		FLWO	0.6	<i>R</i>	15.39*	0.01	
		FLWO	0.6	<i>R</i>	15.44*	0.01	
		FLWO	0.6	<i>I</i>	15.27*	0.01	
		FLWO	0.7	<i>R</i>	15.48*	0.01	
		FLWO	0.7	<i>I</i>	15.3*	0.01	
		FLWO	0.7	<i>R</i>	15.52*	0.01	
		FLWO	0.7	<i>I</i>	15.35*	0.01	
		KAIT	0.7	<i>R</i>	15.61*	0.03	
		FLWO	0.7	<i>R</i>	15.59*	0.01	
		FLWO	0.7	<i>I</i>	15.39*	0.01	
		KAIT	0.7	<i>I</i>	15.42*	0.03	
		FLWO	0.7	<i>R</i>	15.6*	0.01	
		FLWO	0.7	<i>I</i>	15.43*	0.01	
		KAIT	0.7	<i>R</i>	15.63*	0.02	
		FLWO	0.7	<i>R</i>	15.63*	0.01	
		KAIT	0.7	<i>I</i>	15.44*	0.03	
		FLWO	0.7	<i>I</i>	15.5*	0.01	
		FLWO	0.7	<i>R</i>	15.67*	0.01	
		FLWO	0.7	<i>I</i>	15.5*	0.01	
		KAIT	0.7	<i>R</i>	15.67*	0.01	
		KAIT	0.7	<i>I</i>	15.48*	0.02	
		FLWO	0.7	<i>R</i>	15.71	0.01	
		FLWO	0.7	<i>I</i>	15.49	0.01	
		FLWO	0.7	<i>R</i>	15.71	0.01	
		FLWO	0.7	<i>I</i>	15.55	0.01	
		FLWO	0.8	<i>R</i>	15.74	0.01	
		FLWO	0.8	<i>I</i>	15.58	0.01	
		FLWO	0.8	<i>R</i>	15.79	0.01	
		KAIT	0.8	<i>R</i>	15.8	0.02	
		FLWO	0.8	<i>I</i>	15.62	0.01	
		KAIT	0.8	<i>I</i>	15.58	0.03	
		FLWO	0.8	<i>R</i>	15.79	0.01	
		FLWO	0.8	<i>I</i>	15.63	0.01	
		KAIT	0.8	<i>R</i>	15.84	0.02	
		KAIT	0.8	<i>I</i>	15.67	0.03	
		FLWO	0.8	<i>R</i>	15.83	0.01	
FLWO	0.8	<i>I</i>	15.68	0.01			
FLWO	0.8	<i>R</i>	15.84	0.01			

Table 2 continued

Table 2 (*continued*)

GRB	z	Tel./Instum.	δt_{rest} (days)	Filter	Magnitude [†] (AB mag)	Error (AB mag)	Reference
		FLWO	0.8	<i>I</i>	15.67	0.02	
		FLWO	0.8	<i>R</i>	15.87	0.01	
		FLWO	0.8	<i>I</i>	15.68	0.02	
		FLWO	0.8	<i>R</i>	15.91	0.01	
		FLWO	0.8	<i>I</i>	15.74	0.01	
		KAIT	0.8	<i>R</i>	15.91	0.01	
		KAIT	0.8	<i>I</i>	15.74	0.02	
		FLWO	0.8	<i>R</i>	15.96*	0.01	
		FLWO	0.8	<i>I</i>	15.78*	0.01	
		FLWO	0.8	<i>R</i>	15.95*	0.01	
		FLWO	0.8	<i>I</i>	15.8*	0.02	
		KAIT	0.8	<i>R</i>	16.0*	0.08	
		KAIT	0.8	<i>I</i>	15.75	0.03	
		FLWO	0.8	<i>R</i>	15.98*	0.01	
		FLWO	0.9	<i>I</i>	15.83*	0.01	
		FLWO	0.9	<i>R</i>	16.01*	0.01	
		FLWO	0.9	<i>I</i>	15.87*	0.02	
		KAIT	0.9	<i>R</i>	16.01*	0.01	
		KAIT	0.9	<i>I</i>	15.85*	0.02	
		FLWO	0.9	<i>R</i>	16.06*	0.01	
		FLWO	0.9	<i>I</i>	15.86*	0.02	
		KAIT	0.9	<i>R</i>	16.08*	0.01	
		KAIT	0.9	<i>I</i>	15.87*	0.02	
		FLWO	0.9	<i>R</i>	16.08*	0.01	
		FLWO	0.9	<i>I</i>	15.86*	0.02	
		FLWO	0.9	<i>R</i>	16.1*	0.01	
		FLWO	0.9	<i>I</i>	15.87*	0.02	
		KAIT	0.9	<i>R</i>	16.09*	0.02	
		KAIT	0.9	<i>I</i>	15.92*	0.02	
		FLWO	0.9	<i>R</i>	16.12*	0.01	
		FLWO	0.9	<i>I</i>	15.89*	0.02	
		FLWO	0.9	<i>R</i>	16.16*	0.01	
		KAIT	0.9	<i>R</i>	16.13*	0.02	
		FLWO	0.9	<i>I</i>	15.96*	0.02	
		KAIT	0.9	<i>I</i>	15.98*	0.02	
		FLWO	0.9	<i>R</i>	16.19*	0.02	
		FLWO	0.9	<i>I</i>	16.06*	0.02	
		KAIT	0.9	<i>R</i>	16.15*	0.02	
		KAIT	0.9	<i>I</i>	16.02*	0.04	
		FLWO	0.9	<i>R</i>	16.21*	0.02	
		FLWO	0.9	<i>I</i>	16.1*	0.02	
		FLWO	0.9	<i>R</i>	16.24*	0.02	
		FLWO	0.9	<i>I</i>	16.1*	0.02	
		KAIT	0.9	<i>R</i>	16.29*	0.06	
		KAIT	0.9	<i>I</i>	16.02*	0.03	

Table 2 *continued*

Table 2 (*continued*)

GRB	z	Tel./Instum.	δt_{rest} (days)	Filter	Magnitude [†] (AB mag)	Error (AB mag)	Reference
		FLWO	1.0	<i>R</i>	16.28*	0.02	
		FLWO	1.0	<i>I</i>	16.1*	0.03	
		Clay	1.6	<i>R</i>	16.44	0.02	
		Clay	1.6	<i>R</i>	16.44	0.02	
		Clay	1.6	<i>R</i>	16.43	0.02	
		Clay	1.6	<i>R</i>	16.44	0.02	
		FLWO	1.7	<i>R</i>	16.48	0.01	
		FLWO	1.7	<i>I</i>	16.28	0.01	
		FLWO	1.7	<i>R</i>	16.61	0.01	
		FLWO	1.7	<i>I</i>	16.4	0.01	
		KAIT	1.8	<i>R</i>	16.75	0.02	
		KAIT	1.8	<i>I</i>	16.49	0.04	
		FLWO	1.8	<i>R</i>	16.75	0.01	
		FLWO	1.8	<i>I</i>	16.54	0.01	
		KAIT	1.9	<i>R</i>	16.86	0.07	
		KAIT	1.9	<i>I</i>	16.51	0.07	
		FLWO	1.9	<i>R</i>	16.78	0.01	
		FLWO	1.9	<i>I</i>	16.57	0.01	
		Clay	2.6	<i>R</i>	17.02	0.02	
		Clay	2.6	<i>R</i>	17.06	0.02	
		Clay	2.6	<i>R</i>	17.07	0.02	
		Clay	2.6	<i>R</i>	17.07	0.02	
		FLWO	2.9	<i>R</i>	17.28	0.01	
		FLWO	2.9	<i>I</i>	17.04	0.01	
		FLWO	3.0	<i>R</i>	17.36	0.01	
		FLWO	3.0	<i>I</i>	17.13	0.02	
		Clay	3.6	<i>R</i>	17.45	0.02	
		Clay	3.6	<i>R</i>	17.45	0.02	
		Clay	3.6	<i>R</i>	17.46	0.02	
		Clay	3.6	<i>R</i>	17.45	0.02	
		Clay	3.6	<i>R</i>	17.46	0.02	
		LCO40	3.6	<i>J</i>	16.84	0.02	
		Clay	3.6	<i>R</i>	17.44	0.02	
		LCO40	3.6	<i>H</i>	16.61	0.02	
		FLWO	3.7	<i>R</i>	17.57	0.03	
		FLWO	3.8	<i>R</i>	17.6	0.02	
		FLWO	3.8	<i>I</i>	17.41	0.02	
		FLWO	3.8	<i>R</i>	17.62	0.01	
		FLWO	3.8	<i>I</i>	17.43	0.02	
		FLWO	3.8	<i>R</i>	17.64	0.01	
		FLWO	3.8	<i>I</i>	17.42	0.02	
		FLWO	3.8	<i>R</i>	17.67	0.01	
		FLWO	3.8	<i>I</i>	17.46	0.02	
		FLWO	3.9	<i>R</i>	17.7	0.02	
		FLWO	3.9	<i>I</i>	17.48	0.05	

Table 2 (*continued*)

Table 2 (*continued*)

GRB	z	Tel./Instum.	δt_{rest} (days)	Filter	Magnitude [†] (AB mag)	Error (AB mag)	Reference
		Clay	4.6	<i>R</i>	18.01	0.02	
		Clay	4.6	<i>R</i>	18.0	0.02	
		Clay	4.6	<i>R</i>	18.0	0.02	
		Clay	4.6	<i>R</i>	18.0	0.02	
		Clay	4.6	<i>R</i>	18.01	0.02	
		Clay	4.6	<i>R</i>	18.01	0.02	
		Clay	4.6	<i>R</i>	18.02	0.02	
		Clay	4.6	<i>R</i>	18.01	0.02	
		Clay	4.6	<i>R</i>	18.04	0.02	
		LCO40	4.6	<i>J</i>	17.36	0.03	
		FLWO	4.7	<i>R</i>	18.0	0.02	
		FLWO	4.7	<i>I</i>	17.81	0.02	
		LCO40	4.7	<i>H</i>	16.96	0.03	
		FLWO	5.6	<i>R</i>	17.99	0.02	
		FLWO	5.6	<i>I</i>	17.77	0.02	
		LCO40	5.7	<i>J</i>	17.33	0.02	
		LCO40	5.7	<i>H</i>	17.08	0.03	
		LCO100	5.7	<i>I</i>	17.82	0.02	
		LCO100	5.7	<i>I</i>	17.82	0.02	
		LCO100	6.6	<i>I</i>	18.28	0.02	
		LCO100	6.6	<i>I</i>	18.33	0.03	
		LCO40	6.6	<i>J</i>	17.96	0.04	
		LCO40	6.6	<i>H</i>	17.59	0.04	
		FLWO	6.7	<i>R</i>	18.46	0.02	
		FLWO	6.7	<i>I</i>	18.35	0.03	
		FLWO	6.9	<i>R</i>	18.6	0.02	
		FLWO	6.9	<i>I</i>	18.42	0.03	
		FLWO	7.6	<i>R</i>	18.94	0.03	
		FLWO	7.7	<i>I</i>	18.76	0.04	
		LCO40	7.7	<i>H</i>	18.02	0.05	
		LCO40	7.7	<i>J</i>	18.35	0.03	
		FLWO	7.9	<i>R</i>	18.96	0.04	
		FLWO	7.9	<i>I</i>	18.84	0.05	
		LCO40	8.6	<i>J</i>	18.47	0.04	
		FLWO	8.6	<i>R</i>	19.06	0.03	
		FLWO	8.6	<i>I</i>	18.92	0.04	
		LCO40	8.7	<i>H</i>	18.22	0.08	
		FLWO	8.7	<i>R</i>	19.04	0.04	
		FLWO	8.8	<i>R</i>	19.06	0.03	
		FLWO	8.8	<i>I</i>	18.92	0.04	
		FLWO	8.9	<i>R</i>	19.09	0.03	
		FLWO	8.9	<i>I</i>	18.97	0.05	
		FLWO	9.6	<i>R</i>	19.1	0.03	
		LCO40	9.6	<i>J</i>	18.65	0.04	
		FLWO	9.6	<i>I</i>	19.05	0.05	

Table 2 (*continued*)

Table 2 (*continued*)

GRB	z	Tel./Instum.	δt_{rest} (days)	Filter	Magnitude [†] (AB mag)	Error (AB mag)	Reference
		LCO40	9.7	<i>H</i>	18.54	0.05	
		FLWO	9.8	<i>R</i>	19.14	0.03	
		FLWO	9.8	<i>I</i>	18.98	0.04	
		FLWO	9.9	<i>R</i>	19.15	0.04	
		FLWO	9.9	<i>I</i>	19.03	0.06	
		FLWO	10.7	<i>R</i>	19.31	0.04	
		FLWO	10.7	<i>I</i>	19.19	0.05	
		FLWO	10.8	<i>I</i>	19.22	0.04	
		FLWO	10.8	<i>R</i>	19.26	0.03	
		LCO40	11.6	<i>J</i>	19.14	0.07	
		FLWO	11.7	<i>R</i>	19.46	0.03	
		FLWO	11.7	<i>I</i>	19.36	0.04	
		FLWO	11.7	<i>R</i>	19.42	0.03	
		FLWO	11.7	<i>I</i>	19.39	0.05	
		FLWO	11.8	<i>R</i>	19.47	0.03	
		FLWO	11.8	<i>I</i>	19.43	0.06	
		FLWO	12.7	<i>R</i>	19.52	0.03	
		FLWO	12.8	<i>R</i>	19.57	0.04	
		FLWO	13.6	<i>R</i>	19.62	0.08	
		FLWO	13.7	<i>R</i>	19.69	0.08	
		HST/WFPC2	17.0	<i>F606W</i>	20.14	0.002	This work
		HST/WFPC2	17.5	<i>F814W</i>	20.01	0.0	This work
		FLWO	19.7	<i>R</i>	19.99	0.04	Matheson et al. (2003)
		FLWO	19.7	<i>R</i>	20.02	0.04	
		FLWO	19.8	<i>R</i>	20.02	0.06	
		FLWO	20.7	<i>R</i>	20.07	0.04	
		FLWO	20.8	<i>R</i>	20.15	0.05	
		FLWO	20.8	<i>R</i>	20.0	0.05	
		FLWO	21.7	<i>R</i>	20.15	0.03	
		FLWO	21.8	<i>R</i>	20.16	0.04	
		FLWO	21.9	<i>R</i>	20.08	0.06	
		LCO40	22.6	<i>R</i>	20.16	0.05	
		FLWO	22.6	<i>R</i>	20.23	0.04	
		HST/NICMOS/NIC2	22.7	<i>F110W</i>	20.47	0.0	This work
		FLWO	22.7	<i>R</i>	20.22	0.04	Matheson et al. (2003)
		HST/NICMOS/NIC2	22.8	<i>F160W</i>	20.6	0.0	This work
		HST/WFPC2	23.1	<i>F606W</i>	20.39	0.0	This work
		HST/WFPC2	23.2	<i>F814W</i>	20.31	0.0	This work
		FLWO	23.7	<i>R</i>	20.29	0.03	Matheson et al. (2003)
		FLWO	23.8	<i>R</i>	20.25	0.04	
		FLWO	24.7	<i>R</i>	20.36	0.04	
		FLWO	24.8	<i>R</i>	20.33	0.03	
		KPNO4m	25.7	<i>R</i>	20.37	0.02	
		FLWO	25.7	<i>R</i>	20.35	0.04	
		KPNO4m	25.7	<i>R</i>	20.36	0.02	

Table 2 (*continued*)

Table 2 (*continued*)

GRB	z	Tel./Instum.	δt_{rest} (days)	Filter	Magnitude [†] (AB mag)	Error (AB mag)	Reference
		FLWO	25.7	<i>R</i>	20.39	0.04	
		FLWO	26.7	<i>R</i>	20.46	0.04	
		FLWO	27.7	<i>R</i>	20.53	0.05	
		FLWO	28.7	<i>R</i>	20.44	0.05	
		FLWO	28.7	<i>R</i>	20.56	0.06	
		FLWO	29.7	<i>R</i>	20.63	0.04	
		FLWO	29.7	<i>R</i>	20.56	0.04	
		FLWO	29.7	<i>R</i>	20.63	0.05	
		FLWO	30.7	<i>R</i>	20.69	0.04	
		FLWO	30.7	<i>R</i>	20.7	0.04	
		FLWO	31.7	<i>R</i>	20.78	0.04	
		LCO40	32.6	<i>R</i>	20.76	0.07	
		FLWO	32.7	<i>R</i>	20.8	0.04	
		KPNO4m	33.6	<i>R</i>	20.88	0.03	
		FLWO	33.8	<i>R</i>	20.77	0.06	
		FLWO	33.8	<i>R</i>	20.87	0.06	
		KPNO4m	34.6	<i>R</i>	20.91	0.04	
		FLWO	34.7	<i>R</i>	21.02	0.07	
		FLWO	34.7	<i>R</i>	20.92	0.05	
		FLWO	36.8	<i>R</i>	21.08	0.08	
		FLWO	37.7	<i>R</i>	21.03	0.07	
		FLWO	37.7	<i>R</i>	21.11	0.05	
		FLWO	37.7	<i>R</i>	21.03	0.06	
		FLWO	38.7	<i>R</i>	21.23	0.06	
		FLWO	39.7	<i>R</i>	21.22	0.07	
		HST/WFPC2	43.7	<i>F814W</i>	21.49	0.01	This work
		HST/WFPC2	43.7	<i>F606W</i>	21.9	0.01	This work
		HST/NICMOS/NIC2	45.1	<i>F110W</i>	21.58	0.01	This work
		HST/NICMOS/NIC2	45.2	<i>F160W</i>	21.97	0.01	This work
		FLWO	51.7	<i>R</i>	21.76	0.06	Matheson et al. (2003)
		FLWO	52.7	<i>R</i>	21.91	0.11	
		FLWO	53.7	<i>R</i>	21.64	0.08	
		FLWO	54.7	<i>R</i>	21.52	0.09	
		FLWO	57.7	<i>R</i>	21.82	0.06	
		FLWO	59.7	<i>R</i>	21.67	0.07	
		FLWO	60.7	<i>R</i>	21.83	0.09	
		HST/WFPC2	72.9	<i>F814W</i>	22.3	0.01	This work
		HST/WFPC2	73.6	<i>F606W</i>	22.75	0.01	This work
		HST/WFPC2	93.3	<i>F814W</i>	22.77	0.01	This work
		HST/WFPC2	93.4	<i>F606W</i>	23.11	0.01	This work
		HST/WFPC2	227.7	<i>F606W</i>	25.39	0.02	This work
		HST/WFPC2	227.8	<i>F814W</i>	24.95	0.04	This work
		HST/WFPC2	422.6	<i>F606W</i>	27.59	0.1	This work
100316D	0.0591	GROND	0.5	<i>r</i>	20.9*	0.04	Olivares E. et al. (2012)
		GROND	0.5	<i>J</i>	20.69*	0.14	

Table 2 *continued*

Table 2 (*continued*)

GRB	z	Tel./Instum.	δt_{rest} (days)	Filter	Magnitude [†] (AB mag)	Error (AB mag)	Reference
		GROND	0.5	<i>i</i>	20.87*	0.05	
		GROND	0.6	<i>J</i>	20.71*	0.26	
		GROND	0.6	<i>r</i>	20.91*	0.03	
		GROND	0.6	<i>i</i>	20.94*	0.04	
		GROND	1.5	<i>r</i>	20.9	0.04	
		GROND	1.5	<i>i</i>	20.59	0.05	
		GROND	1.5	<i>J</i>	20.47	0.22	
		GROND	1.7	<i>i</i>	20.69	0.05	
		GROND	1.7	<i>r</i>	20.77	0.03	
		GROND	2.5	<i>i</i>	20.5	0.05	
		GROND	2.5	<i>r</i>	20.58	0.04	
		GROND	2.5	<i>J</i>	19.99	0.17	
		GROND	3.5	<i>r</i>	20.4	0.03	
		GROND	3.5	<i>i</i>	20.24	0.03	
		GROND	3.5	<i>J</i>	19.72	0.17	
		GROND	3.5	<i>H</i>	19.94	0.21	
		GROND	4.5	<i>J</i>	20.0	0.19	
		GROND	4.5	<i>r</i>	20.21	0.03	
		GROND	4.5	<i>i</i>	20.15	0.04	
		GROND	4.5	<i>H</i>	20.22	0.23	
		GROND	5.5	<i>H</i>	19.92	0.23	
		GROND	5.5	<i>r</i>	20.11	0.04	
		GROND	5.5	<i>i</i>	20.04	0.04	
		GROND	5.5	<i>J</i>	19.93	0.19	
		GROND	7.5	<i>H</i>	20.2	0.28	
		GROND	7.5	<i>r</i>	19.96	0.04	
		GROND	7.5	<i>J</i>	19.69	0.19	
		GROND	7.5	<i>i</i>	19.87	0.06	
		HST/WFC3/UVIS	8.7	<i>F555W</i>	19.99	0.014	This work
		HST/WFC3/UVIS	8.7	<i>F814W</i>	19.45	0.01	This work
		HST/WFC3/IR	8.7	<i>F125W</i>	20.0	0.01	This work
		HST/WFC3/IR	8.7	<i>F160W</i>	20.15	0.01	This work
		GROND	10.5	<i>H</i>	19.85	0.25	Olivares E. et al. (2012)
		GROND	10.5	<i>i</i>	19.98	0.04	
		GROND	10.5	<i>r</i>	19.91	0.03	
		GROND	10.5	<i>J</i>	19.53	0.14	
		GROND	11.5	<i>r</i>	20.01	0.03	
		GROND	11.5	<i>H</i>	19.94	0.18	
		GROND	11.5	<i>J</i>	19.49	0.14	
		GROND	11.5	<i>i</i>	19.99	0.04	
		GROND	14.5	<i>r</i>	20.07	0.03	
		GROND	14.5	<i>i</i>	20.08	0.03	
		GROND	14.5	<i>J</i>	19.51	0.12	
		GROND	14.5	<i>H</i>	19.67	0.22	
		GROND	15.5	<i>i</i>	20.16	0.05	

Table 2 *continued*

Table 2 (*continued*)

GRB	z	Tel./Instum.	δt_{rest} (days)	Filter	Magnitude [†] (AB mag)	Error (AB mag)	Reference
		GROND	15.5	H	19.85	0.19	
		GROND	15.5	r	20.07	0.04	
		GROND	15.5	J	19.59	0.13	
		HST/WFC3/UVIS	15.8	$F555W$	20.51	0.02	This work
		HST/WFC3/UVIS	15.8	$F814W$	19.57	0.01	This work
		GROND	19.5	J	19.7	0.19	Olivares E. et al. (2012)
		GROND	19.5	r	20.36	0.05	
		GROND	19.5	i	20.39	0.07	
		GROND	21.5	J	19.64	0.13	
		GROND	21.5	i	20.48	0.04	
		GROND	21.5	H	19.95	0.19	
		GROND	21.5	r	20.48	0.04	
		HST/WFC3/UVIS	24.9	$F555W$	21.07	0.02	This work
		HST/WFC3/UVIS	24.9	$F814W$	20.03	0.01	This work
		HST/WFC3/IR	25.5	$F125W$	20.08	0.01	This work
		GROND	25.5	J	19.67	0.13	Olivares E. et al. (2012)
		GROND	25.5	H	20.3	0.21	
		GROND	25.5	i	20.66	0.03	
		GROND	25.5	r	20.78	0.03	
		HST/WFC3/IR	25.5	$F160W$	20.03	0.01	This work
		GROND	32.5	r	21.42	0.04	Olivares E. et al. (2012)
		GROND	32.5	J	20.07	0.19	
		GROND	32.5	i	21.28	0.05	
		GROND	40.5	i	21.74	0.07	
		GROND	40.5	r	21.83	0.06	
		HST/WFC3/UVIS	47.4	$F555W$	22.57	0.03	This work
		HST/WFC3/UVIS	47.4	$F814W$	21.43	0.02	This work
		GROND	83.4	r	23.66	0.23	Olivares E. et al. (2012)
		HST/WFC3/UVIS	137.5	$F555W$	24.62	0.03	This work
		HST/WFC3/UVIS	137.5	$F814W$	23.55	0.04	This work
130427A	0.3399	GROND	1.7	r	18.61*	0.04	Perley et al. (2014)
		GROND	1.7	i	18.47*	0.05	
		GROND	1.7	J	18.09*	0.05	
		GROND	1.7	H	18.07*	0.07	
		GROND	1.7	K	17.72*	0.07	
		P60	1.8	r	18.7*	0.04	
		P60	1.8	i	18.56	0.05	
		P60	1.8	r	18.73*	0.02	
		P60	1.9	i	18.54*	0.04	
		P60	1.9	r	18.74*	0.02	
		P60	1.9	i	18.59*	0.05	
		KAIT	1.9	R	18.81	0.05	
		P60	1.9	r	18.75*	0.03	
		KAIT	1.9	I	18.68	0.08	
		RATIR	1.9	H	18.09*	0.05	

Table 2 *continued*

Table 2 (*continued*)

GRB	z	Tel./Instum.	δt_{rest} (days)	Filter	Magnitude [†] (AB mag)	Error (AB mag)	Reference
		RATIR	1.9	<i>J</i>	18.27*	0.05	
		P60	1.9	<i>i</i>	18.58*	0.05	
		P60	1.9	<i>r</i>	18.77*	0.03	
		P60	1.9	<i>i</i>	18.6*	0.05	
		P60	1.9	<i>r</i>	18.8*	0.02	
		P60	1.9	<i>i</i>	18.55*	0.05	
		P60	1.9	<i>r</i>	18.8*	0.03	
		P60	1.9	<i>i</i>	18.59*	0.05	
		P60	1.9	<i>r</i>	18.82*	0.03	
		P60	1.9	<i>i</i>	18.59*	0.06	
		P60	2.0	<i>r</i>	18.81*	0.03	
		P60	2.0	<i>r</i>	18.85	0.04	
		P60	2.0	<i>i</i>	18.66*	0.05	
		P60	2.0	<i>r</i>	18.88	0.03	
		P60	2.0	<i>i</i>	18.71*	0.05	
		P60	2.0	<i>r</i>	18.85	0.03	
		P60	2.0	<i>i</i>	18.67*	0.05	
		P60	2.0	<i>r</i>	18.89*	0.03	
		P60	2.0	<i>i</i>	18.68*	0.05	
		P60	2.0	<i>r</i>	18.85*	0.03	
		P60	2.0	<i>i</i>	18.67*	0.05	
		P60	2.0	<i>r</i>	18.88*	0.04	
		P60	2.0	<i>i</i>	18.72*	0.05	
		P60	2.0	<i>r</i>	18.91*	0.04	
		P60	2.1	<i>i</i>	18.74*	0.05	
		P60	2.1	<i>r</i>	18.91*	0.04	
		P60	2.1	<i>i</i>	18.73*	0.07	
		P60	2.1	<i>r</i>	18.93*	0.05	
		P60	2.1	<i>i</i>	18.68*	0.07	
		P60	2.1	<i>r</i>	18.89*	0.05	
		GMG	2.2	<i>r</i>	19.02*	0.03	
		GMG	2.2	<i>r</i>	19.05*	0.03	
		GMG	2.2	<i>r</i>	19.06*	0.03	
		T100	2.6	<i>R</i>	19.07	0.05	
		P60	2.8	<i>r</i>	19.37*	0.03	
		P60	2.8	<i>i</i>	19.2*	0.06	
		P60	2.8	<i>r</i>	19.37*	0.04	
		KAIT	2.9	<i>R</i>	19.59	0.12	
		KAIT	2.9	<i>I</i>	18.77	0.15	
		P60	2.9	<i>r</i>	19.39*	0.03	
		P60	2.9	<i>i</i>	19.15*	0.09	
		P60	2.9	<i>r</i>	19.44*	0.03	
		P60	2.9	<i>i</i>	19.29*	0.07	
		RATIR	2.9	<i>H</i>	18.71*	0.06	
		RATIR	2.9	<i>J</i>	19.05*	0.06	

Table 2 (*continued*)

Table 2 (*continued*)

GRB	z	Tel./Instum.	δt_{rest} (days)	Filter	Magnitude [†] (AB mag)	Error (AB mag)	Reference
		P60	2.9	r	19.44*	0.03	
		P60	3.0	i	19.3*	0.07	
		P60	3.0	r	19.48*	0.03	
		P60	3.0	i	19.26*	0.07	
		P60	3.0	r	19.43*	0.04	
		P60	3.0	i	19.35*	0.08	
		P60	3.0	r	19.49*	0.03	
		P60	3.0	i	19.17*	0.06	
		P60	3.0	r	19.48*	0.05	
		UKIRT	3.0	K	18.53*	0.03	
		P60	3.0	i	19.3*	0.07	
		UKIRT	3.0	H	18.73*	0.03	
		P60	3.1	r	19.52*	0.04	
		P60	3.1	i	19.34*	0.07	
		UKIRT	3.1	J	18.96*	0.03	
		P60	3.1	r	19.43*	0.05	
		GMG	3.3	r	19.63*	0.04	
		GMG	3.3	r	19.66*	0.04	
		T100	3.4	R	19.81	0.07	
		P60	3.8	r	19.78*	0.05	
		P60	3.8	i	19.58*	0.08	
		P60	3.8	r	19.86*	0.04	
		P60	3.9	i	19.59*	0.09	
		Nickel	3.9	R	19.61	0.12	
		Nickel	3.9	I	19.78	0.12	
		P60	3.9	r	19.83*	0.05	
		P60	3.9	i	19.71*	0.1	
		P60	3.9	r	19.85*	0.05	
		P60	3.9	i	19.62*	0.09	
		P60	3.9	r	19.88*	0.05	
		P60	3.9	i	19.78*	0.1	
		P60	3.9	r	19.87*	0.07	
		P60	3.9	r	19.89*	0.06	
		P60	3.9	i	19.66*	0.1	
		P60	4.0	r	19.92*	0.05	
		P60	4.0	i	19.61*	0.09	
		P60	4.0	r	19.92*	0.05	
		P60	4.0	i	19.64*	0.09	
		P60	4.0	r	19.88*	0.05	
		P60	4.0	i	19.66*	0.08	
		P60	4.0	r	19.82*	0.05	
		P60	4.0	i	19.64*	0.08	
		P60	4.0	r	19.92*	0.04	
		P60	4.0	i	19.68*	0.1	
		P60	4.1	r	19.86*	0.05	

Table 2 *continued*

Table 2 (*continued*)

GRB	z	Tel./Instum.	δt_{rest} (days)	Filter	Magnitude [†] (AB mag)	Error (AB mag)	Reference
		P60	4.1	<i>i</i>	19.64*	0.1	
		T100	4.6	<i>R</i>	20.14	0.07	
		P60	4.9	<i>r</i>	20.24*	0.06	
		P60	4.9	<i>i</i>	19.91*	0.1	
		P60	4.9	<i>r</i>	20.19*	0.04	
		P60	4.9	<i>i</i>	19.96*	0.07	
		KAST	4.9	<i>R</i>	20.35	0.14	
		KAST	4.9	<i>R</i>	20.26	0.03	
		UKIRT	5.0	<i>K</i>	19.24*	0.04	
		UKIRT	5.0	<i>J</i>	19.56*	0.05	
		P60	5.0	<i>r</i>	20.24*	0.05	
		P60	5.0	<i>i</i>	19.94*	0.1	
		T100	5.5	<i>R</i>	20.43	0.08	
		P60	6.0	<i>r</i>	20.5*	0.05	
		P60	6.0	<i>i</i>	20.14*	0.09	
		P60	7.0	<i>r</i>	20.62*	0.05	
		P60	7.0	<i>i</i>	20.47*	0.1	
		UKIRT	7.9	<i>K</i>	19.9*	0.06	
		UKIRT	7.9	<i>H</i>	20.24*	0.07	
		UKIRT	7.9	<i>J</i>	20.35*	0.08	
		P60	8.0	<i>r</i>	20.76*	0.07	
		P60	8.0	<i>i</i>	20.48*	0.12	
		Tautenburg	8.6	<i>R</i>	21.04	0.15	
		UKIRT	11.9	<i>K</i>	20.57*	0.09	
		UKIRT	11.9	<i>H</i>	20.84*	0.12	
		UKIRT	11.9	<i>J</i>	20.93*	0.13	
		P60	13.0	<i>r</i>	21.33*	0.1	
		Keck	13.1	<i>R</i>	21.47	0.07	
		P60	13.9	<i>r</i>	21.28*	0.05	
		P60	14.0	<i>i</i>	21.03*	0.14	
		P60	14.8	<i>r</i>	21.33*	0.07	
		P60	14.9	<i>i</i>	21.08*	0.15	
		Tautenburg	15.5	<i>R</i>	21.58	0.18	
		P60	15.9	<i>r</i>	21.42*	0.08	
		P60	15.9	<i>i</i>	21.25*	0.18	
		UKIRT	15.9	<i>K</i>	20.85	0.1	
		UKIRT	16.0	<i>H</i>	21.04	0.16	
		UKIRT	16.0	<i>J</i>	21.09	0.14	
		GROND	16.7	<i>r</i>	21.81*	0.09	
		GROND	16.7	<i>i</i>	21.48	0.17	
		P60	17.0	<i>i</i>	21.13	0.15	
		P60	17.0	<i>r</i>	21.69*	0.1	
		P60	17.9	<i>i</i>	21.16	0.16	
		P60	18.0	<i>r</i>	21.5*	0.09	
		P200	18.0	<i>r</i>	21.69*	0.24	

Table 2 *continued*

Table 2 (continued)

GRB	z	Tel./Instum.	δt_{rest} (days)	Filter	Magnitude [†] (AB mag)	Error (AB mag)	Reference
		GROND	18.7	<i>i</i>	21.68	0.21	
		GROND	18.7	<i>r</i>	21.79*	0.11	
		Gemini-N	18.9	<i>i</i>	21.76	0.21	
		Gemini-N	18.9	<i>r</i>	21.99*	0.12	
		P60	18.9	<i>i</i>	21.2	0.16	
		P60	19.0	<i>r</i>	21.75*	0.1	
		P60	20.0	<i>i</i>	20.91	0.24	
		Gemini-N	20.0	<i>r</i>	21.79*	0.21	
		P60	20.0	<i>r</i>	21.75*	0.11	
		UKIRT	20.9	<i>K</i>	21.4*	0.17	
		UKIRT	20.9	<i>H</i>	21.13	0.16	
		UKIRT	21.0	<i>J</i>	21.57	0.23	
		HST/WFC3/IR	22.8	<i>F160W</i>	21.74	0.014	This work
		P60	22.9	<i>i</i>	21.41	0.2	Perley et al. (2014)
		P60	22.9	<i>r</i>	21.78	0.12	
		UKIRT	23.0	<i>K</i>	21.56*	0.19	
		HST/WFC3/UVIS	23.0	<i>F606W</i>	21.87	0.01	This work
		UKIRT	23.1	<i>J</i>	21.41	0.18	Perley et al. (2014)
		P60	23.9	<i>i</i>	21.3	0.21	
		P60	23.9	<i>r</i>	21.72	0.14	
		P60	24.9	<i>i</i>	21.3	0.2	
		P60	26.9	<i>i</i>	21.63	0.26	
		UKIRT	30.0	<i>J</i>	21.73	0.26	
		P60	32.9	<i>r</i>	22.53	0.17	
		P60	34.9	<i>i</i>	21.94	0.27	
		P60	36.9	<i>r</i>	22.65	0.17	
		P60	39.9	<i>i</i>	21.88	0.21	
		Keck	40.0	<i>R</i>	23.18	0.22	
		UKIRT	40.9	<i>H</i>	21.45	0.18	
		HST/WFC3/IR	73.9	<i>F160W</i>	23.06	0.02	This work
		HST/WFC3/UVIS	73.9	<i>F606W</i>	23.96	0.02	This work
		HST/WFC3/IR	259.8	<i>F160W</i>	25.71*	0.14	This work
		HST/WFC3/UVIS	259.9	<i>F606W</i>	26.39*	0.07	This work
		HST/WFC3/UVIS	315.9	<i>F606W</i>	26.71*	0.06	This work
		HST/WFC3/IR	316.0	<i>F160W</i>	26.05*	0.11	This work
		HST/WFC3/UVIS	355.9	<i>F606W</i>	26.98*	0.19	This work
		HST/WFC3/IR	382.8	<i>F160W</i>	26.84*	0.17	This work
		HST/WFC3/UVIS	382.9	<i>F606W</i>	27.56*	0.12	This work
		HST/WFC3/IR	587.5	<i>F160W</i>	28.11*	0.64	This work
		HST/WFC3/UVIS	587.6	<i>F606W</i>	27.88*	0.12	This work
190829A	0.0785	GTC	0.4	<i>i</i>	18.87	0.01	Hu et al. (2021)
		GTC	0.4	<i>r</i>	19.79*	0.01	
		GTC	1.4	<i>r</i>	21.86*	0.06	
		GTC	1.4	<i>i</i>	20.81*	0.05	
		GTC	2.4	<i>i</i>	22.42*	0.06	

Table 2 continued

Table 2 (*continued*)

GRB	z	Tel./Instum.	δt_{rest} (days)	Filter	Magnitude [†] (AB mag)	Error (AB mag)	Reference
		GTC	2.4	r	22.71*	0.03	
		GTC	3.4	r	23.05*	0.03	
		GTC	3.4	i	22.38*	0.02	
		GTC	4.4	i	22.23*	0.08	
		GTC	4.4	r	22.7	0.06	
		GTC	7.3	i	22.08	0.04	
		GTC	11.4	i	21.16	0.03	
		GTC	14.3	i	20.84	0.09	
		VLT/HAWKI	25.4	J	19.86	0.021	This work
		VLT/XSHOOTER	25.4	r	22.15	0.12	This work
		VLT/HAWKI	25.4	H	20.22	0.09	This work
		VLT/HAWKI	25.4	K_s	20.19	0.06	This work
		HST/WFC3/IR	29.3	$F110W$	20.28	0.05	This work
		GTC	29.3	i	21.31	0.02	Hu et al. (2021)
		HST/WFC3/IR	29.4	$F160W$	20.51	0.09	This work
		GTC	40.3	i	22.56	0.01	Hu et al. (2021)
		VLT/HAWKI	49.4	J	21.4	0.02	This work
		VLT/HAWKI	49.4	H	21.4	0.08	This work
		VLT/HAWKI	49.4	K_s	21.35	0.07	This work
		VLT/XSHOOTER	50.3	r	23.05	0.17	This work
		HST/WFC3/IR	57.8	$F110W$	21.91	0.12	This work
		HST/WFC3/IR	58.0	$F160W$	21.98	0.18	This work
		VLT/HAWKI	77.2	J	22.25	0.04	This work
		VLT/HAWKI	77.2	H	22.86	0.18	This work
		VLT/HAWKI	77.2	K_s	22.97	0.15	This work
		VLT/XSHOOTER	79.3	r	24.13	0.14	This work
		HST/WFC3/UVIS	87.2	$F606W$	24.71	0.03	This work
		HST/WFC3/IR	92.9	$F140W$	23.55	0.04	This work
		VLT/HAWKI	94.4	K_s	23.68	0.28	This work
		VLT/XSHOOTER	109.2	r	24.81	0.19	This work
		VLT/HAWKI	112.2	J	23.27	0.18	This work
		HST/WFC3/UVIS	135.6	$F606W$	25.34	0.03	This work
		HST/WFC3/IR	135.8	$F140W$	24.17	0.05	This work
		VLT/HAWKI	137.3	J	23.74	0.2	This work
		HST/WFC3/IR	170.4	$F140W$	25.16	0.08	This work
		HST/WFC3/UVIS	170.5	$F606W$	25.96	0.06	This work
		HST/WFC3/IR	299.3	$F140W$	26.4	0.19	This work
		HST/WFC3/UVIS	299.4	$F606W$	27.33	0.27	This work
		HST/WFC3/IR	358.0	$F140W$	26.78	0.25	This work
		HST/WFC3/UVIS	358.0	$F606W$	28.26	0.56	This work

NOTE— (*) Indicates observation is dominated or significantly affected by afterglow emission.

(†) Observations are not corrected for Galactic nor local extinction.